

REPORT DOCUMENTATION PAGE

APRL-SR-AR-TR-07-0015

The public reporting burden for this collection of information is estimated to average 1 hour per response, including the gathering and maintaining the data needed, and completing and reviewing the collection of information. Send comments regarding this burden estimate or any other aspect of this collection of information, including suggestions for reducing the burden, to the Department of Defense, Executive Services and Communications Directorate, 1215 Jefferson Davis Highway, Suite 1204, Arlington, VA 22202-4302, and to the Office of Management and Budget, Paperwork Project Director, Paperwork Project, Washington, DC 20503.

PLEASE DO NOT RETURN YOUR FORM TO THE ABOVE ORGANIZATION.

1. REPORT DATE (DD-MM-YYYY) 04 JAN 2007		2. REPORT TYPE FINAL REPORT		3. DATES COVERED (From - To) 1 JUL 05 TO 30 SEP 06	
4. TITLE AND SUBTITLE DEVELOPMENT OF AN UNCOOLED PHOTOMECHANIC INFRARED SENSOR BASED ON THE IR ORGAN OF THE PYROPHILOUS JEWEL BEETLE MELANOPHILA ACUMINATA				5a. CONTRACT NUMBER	
				5b. GRANT NUMBER FA9550-05-1-0422	
				5c. PROGRAM ELEMENT NUMBER	
6. AUTHOR(S) PROF ALBERT P. PISANO				5d. PROJECT NUMBER	
				5e. TASK NUMBER	
				5f. WORK UNIT NUMBER	
7. PERFORMING ORGANIZATION NAME(S) AND ADDRESS(ES) UNIVERSITY OF CALIFORNIA, BERKELEY DEPT OF MECHANICAL ENGINEERING 6143 ETCHEVERRY HALL #1740, BERKELEY, CA 94720-1740				8. PERFORMING ORGANIZATION REPORT NUMBER	
9. SPONSORING/MONITORING AGENCY NAME(S) AND ADDRESS(ES) AFOSR/NL 875 NORTH RANDOLPH STREET SUITE 325, ROOM 3112 ARLINGTON, VA 22203-1768				10. SPONSOR/MONITOR'S ACRONYM(S)	
				11. SPONSOR/MONITOR'S REPORT NUMBER(S)	
12. DISTRIBUTION/AVAILABILITY STATEMENT <i>Dr. Hugh Delong</i> APPROVE FOR PUBLIC RELEASE: DISTRIBUTION UNLIMITED					
13. SUPPLEMENTARY NOTES					
14. ABSTRACT Initial efforts focused on the MEMS materials development effort including deposition and patterning process for chitosan, and more recent work resulted in the development of a photolithography process for chitosan compatible with traditional microfabrication processes. In order to realize a bio-inspired imaging system based on melanophila acuminata, the polysaccharide chitosan (a water-soluble derivative of chitin which can be reacylated back to chitin through post-processing) was engineered from a commercially available power into a thin film compatible with semiconductor microfabrication processes. Substantial, novel work went into the synthesis, characterization, deposition and patterning of chitosan. MEMS compatible fabrication methods were developed. Controlled deposition of chitosan up to 5 um thick, with uniformity of 10% and roughness of less than 1% has been achieved. Stress temperature curves were recorded from amient to dehydrated conditions showing a clear hysteresis curve which can be exploited for exploited for thermal IR transduction purposes.					
15. SUBJECT TERMS					
16. SECURITY CLASSIFICATION OF:			17. LIMITATION OF ABSTRACT	18. NUMBER OF PAGES	19a. NAME OF RESPONSIBLE PERSON
a. REPORT	b. ABSTRACT	c. THIS PAGE			19b. TELEPHONE NUMBER (Include area code)

**Development of an Uncooled Photomechanic Infrared
Sensor Based on the IR Organ of the Pyrophilous Jewel
Beetle *Melanophila Acuminata***

Lead Organization University of California at Berkeley
Type of Business Other Educational
Technical Area Micro-electromechanical system (MEMS)
Contractor
Establishment Code 87-402-396D
Grant Number FA9550-05-1-0422

**PRINCIPAL
INVESTIGATOR**

Professor Albert P. Pisano
Chair, Department of Mechanical Engineering
University of California, Berkeley TEL: (510) 643-7013
6143 Etcheverry Hall #1740 FAX: (510) 642-6163
Berkeley, CA 94720-1740
appisano@me.berkeley.edu

INVESTIGATORS

Dr. H. Schmitz
University of Bonn, Germany
Professor Luke Lee
University of California, Berkeley

20070201056

Development of an Uncooled Photomechanic Infrared Sensor Based on the IR Organ of the Pyrophilous Jewel Beetle *Melanophila Acuminata*

Table of Contents

Executive Summary	3
University of California, Berkeley (UCB) - Technical Progress Report	7
Chitosan Hydrogel Solution Characterization	7
Chitosan Film Characterization	9
Chitosan Fabrication	13
Chitosan Photolithography	16
Device Processing	27
Device #1: Photomechanical Thin-Film Transistor	27
Device #2: Chitosan-coated MEMS Strain Gauge	37
Device #3: Chitosan Cantilever Infrared Sensor	40
Device #4: Membrane Strain Sensor (Alternate concept).....	46
References	47
Personnel Supported:	48
Interactions & Transitions	48
New Discoveries, Inventions, or Patent Disclosures:	50
University of Bonn - Final Performance Report.....	52
Introductory Remark:	52
People involved in this research:	53
Structure and function of the IR sensilla in <i>Melanophila</i> beetles	54
Material and Methods	56
<i>Animals</i>	56
<i>Scanning electron microscopy</i>	56
<i>Focused ion beam (FIB) technique</i>	56
<i>Light and transmission electron microscopy</i>	56
Infrared receptors in pyrophilous bugs.....	63
Physiology: Electrophysiological recordings	65
Caesar - Final Report IR-Sensor Project	72
1.) Objectives	72
2.) Status of effort	72
Publications:	76

Executive Summary

This report outlines research progress related to the development of an uncooled, low-cost, microelectromechanical (MEMS) sensor for detecting infrared radiation. The work is inspired by the IR imaging system of the pyrophilous jewel beetle *Melanophila acuminata* and has progressed in three main categories: chitosan material characterization and development of a photolithographic patterning process, device modeling and preliminary device fabrication and characterization. This effort began July 1, 2005 and this report covers the entire period of project funding through September 30, 2006.

Initial efforts focused on the MEMS materials development effort including deposition and patterning process for chitosan, and more recent work resulted in the development of a photolithography process for chitosan compatible with traditional microfabrication processes. In order to realize a bio-inspired imaging system based on *Melanophila acuminata*, the polysaccharide chitosan (a water-soluble derivative of chitin which can be reacylated back to chitin through post-processing) was engineered from a commercially available powder into a thin film compatible with semiconductor microfabrication processes. Substantial, novel work went into the synthesis, characterization, deposition and patterning of chitosan. MEMS compatible fabrication methods were developed. Controlled deposition of chitosan up to 5 μm thick, with uniformity of 10% and roughness of less than 1% has been achieved. Stress-temperature curves were recorded from ambient to dehydrated conditions showing a clear hysteresis curve which can be exploited for thermal IR transduction purposes. This work has transformed chitosan into a characterized, repeatable, MEMS engineering material. One of the most significant achievements was the development of a photolithographic patterning process. Concentrated acetic acid has been identified as a wet etchant and oxygen plasma as a dry etchant. Oxygen

plasma etching resulted in high resolution patterning with minimum achievable line widths of 4 μm using contact printing. Resolution is limited by the contact printing equipment rather than the photoresist or lateral chitosan erosion. The process may also be CMOS-compatible, allowing integration of microelectronics with biomimetic chitosan infrared sensors. Demonstrated line widths should be sufficient for development of future IR pixels. Higher resolutions are likely possible using a project printing method.

Two main pixel elements were investigated: a transistor-based (Photomechanical Thin-Film Transistor – PTFT) and a strain-based pixel. Both concepts are based on two primary effects – expansion of chitosan from conformational or thermal effects caused by IR absorption and changes in dielectric constant from conformational changes in bonds in response to IR radiation. For the transistor concept, a chitosan layer deposited on top of a back-gated thin-film transistor (TFT) would induce strain into the channel which would be detected by the transistor from a change in mobility. Also, if chitosan becomes the dielectric of the device, any conformational change could also change the capacitance and therefore affect the output current. A thin-film transistor-based device is advantageous for the pixel element because of its low thermal budget requirement and potential for fabrication on flexible substrates. Another advantage is that interconnect issues are more easily addressed using TFT structures. Preliminary modeling of strain on TFTs was being performed in Medici and Taurus device simulators to determine the potential for utilizing such a device in the final platform. Proof of concept devices and testing was performed by partially replacing the dielectric of NMOS transistors with chitosan. Initial tests show increasing V_T (on-voltage) in response to low intensity IR. Rough calculations indicated a sensitivity or qualitative detectivity to a filtered IR source with a light intensity of $60 \mu\text{W}/\text{cm}^2$, which is similar to the lowest resolvable IR intensity

that *Melanophila acuminata* can detect¹. Drain current (I_d) vs. gate voltage (V_g) operating characteristic curves have shown that for a 1 μm chitosan NMOS transistor with drain voltage bias of 50 mV, operating currents are within the microamp range with current changes due to IR irradiation over 1 μA . The operating currents fit well with current analog/digital circuit design and are well within detectable limits (noise floor is usually in the hundreds of picoamps and currents this low can also be boosted if necessary, similar to memory design). These results are based on unpackaged designs and are carried out in sealed probe stations. Quantitative, calibrated, detectivity measurements have not been conducted.

The second pixel design is based on the measurement of the IR induced strain by the chitosan in the strain-sensing structures. Simulations have been carried out in the Comsol Multi-Physics software package to determine the amount of deflection of a chitosan bimorph structure due to various levels of incoming thermal flux (as an alternative to direct IR since this is not part of the simulation package). A 100 μm long cantilever bimorph of 1 μm thick chitosan and 100 nm of polysilicon irradiated by a 5 mW/cm^2 radiant flux demonstrated an 8.54 μm deflection in the simulation. These results have been used to optimize structures for maximum deflection by increasing thermal expansion mismatch between structural layers. Fabrication of chitosan-polysilicon bimorph structures, as optimized by the modeling effort, is currently in development. It is also hypothesized that a thin metal film deposited in between the chitosan and polysilicon layers could enhance the deflection further by increasing energy absorption in the chitosan layer. Initial characterization will be through optical methods with future instantiations using piezoelectric/resistive materials. Chitin or chitosan coated resonant strain structures can also be used in the final pixel design should extreme sensitivity measurements be required. The Pisano group has previously demonstrated silicon resonant strain structures capable of sensing 30 ne^2 .

Coating these structures with chitosan would offer spectrally sensitive absorption that introduces a strain into the layer. Coupling chitosan into the gauge would produce an infrared sensor where the strain is modulated by the incident infrared flux.

University of California, Berkeley (UCB) - Technical Progress Report

Chitosan Hydrogel Solution Characterization

Current chitosan work utilizes chitosan hydrogel solutions of varying viscosity. The solutions were created by dissolving between 1–6 g of medium molecular weight (MMW) grade chitosan (average molecular weight of 250 kDa) from Sigma-Aldrich into 150 mL of 2:1 buffered acetic acid (deionized water as buffering agent). Vacuum filtering was used to reduce particulate contamination. 5 μm pore membrane filters were used due to the medium to high viscosities of the hydrogels as they were found to be the best balance between time required to filter the solutions and removal of particulates. Simultaneously, the set-up provided degassing of the solution. The chitosan concentrations ranged from 0.66% w/v to 4.0% w/v. Higher chitosan concentrations were not utilized due to the high viscosities achieved with 4.0% w/v and the difficulties associated with processing solutions of higher viscosity.

Increasing the chitosan concentration while keeping the solvent properties constant (pH of 2.33) resulted in increasing pH levels and viscosity. pH was measured using a digital pH meter while viscosity was measured using a rotating cylinder viscometer. From Figure 1a), it can be seen that pH increases linearly with chitosan concentration while viscosity (Figure 1b) has an initial transient before quadratically increasing. This allows for a large range of solution viscosities with a small to moderate change in pH. The pH needs to be controlled to be not too low as later process compatibility as well as CMOS compatibility can be affected by this factor

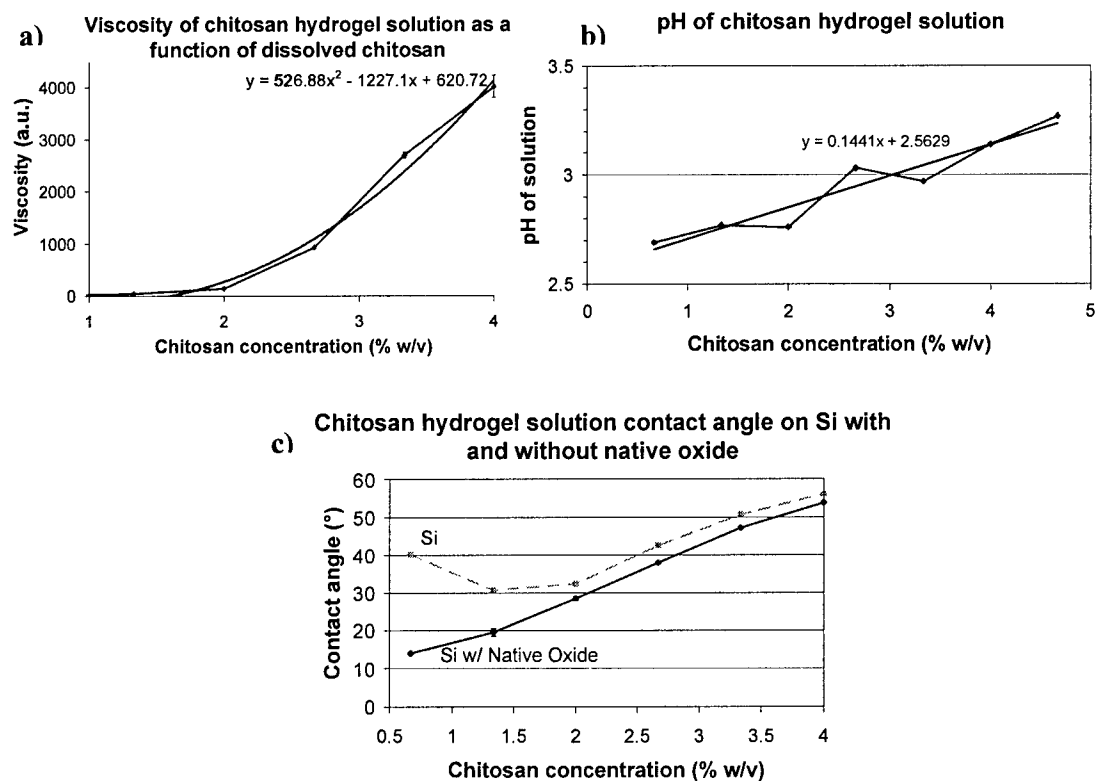


Figure 1. a). pH of chitosan hydrogel solution† with varying concentration of chitosan. b). Viscosity of chitosan hydrogel solution† as the concentration of chitosan is increased. c). Chitosan hydrogel† solution contact angle on bare silicon and silicon with native oxide.

(since direct neutralization using bases can result in fast-diffusing salts being infused into the wafer and damaging CMOS devices). This is the reason why a buffered acetic acid solution was used rather than glacial acetic acid. However, a sufficiently concentrated solution is still needed to ensure formation of a thick gel to increase viscosity. It was found 2:1 buffered acetic acid met this condition well. The resulting chitosan hydrogel viscosities are on the order of viscosities achieved with SU-8 using comparable concentrations of resin to solvent³. Viscosity is important because it plays a role in defining the eventual thickness of the chitosan film, which affects the thickness of a spin-cast film. For thicker films that will better transduce strain expansion of the chitosan films due to IR absorption, higher viscosities are needed.

Another important solution characteristic that determines how the hydrogel solution will be spin-cast is the contact angle the hydrogel makes with the substrate. Solutions with lower contact angle wet the substrate surface better resulting in a better spin. Higher contact angles result in greater hydrophobicity requiring larger amounts of hydrogel to be dispensed to sufficiently cover the substrate surface when spin-cast. However, being a hydrogel, higher contact angles also result in a thicker spin-cast film. The contact angles for various chitosan hydrogels with varying concentrations of chitosan on bare silicon and silicon with native oxide are shown in Figure 1c). Contact angles were measured using the Kruss Contact Angle Analyzer System. While the contact angles increase linearly with increasing chitosan concentration, for even 4.0% w/v of MMW chitosan dissolved, the contact angle remains below 90° for both substrate types resulting in overall hydrophilic wetting allowing for adequate spinning of the hydrogels.

Chitosan Film Characterization

For film characterization, the chitosan solutions were spin-cast onto silicon wafers. Experimentally, it was found that a spin time of 1 minute provided sufficient time for the hydrogel solutions to be spun across the silicon wafers used over a range of spin speeds between 1,000 – 4,500 rpm. The native oxide was kept on the wafers as it provided better wetting of the hydrogel to the wafer surface and would not affect further processing steps. The spin curves for the hydrogel solutions prepared can be found in Figure 2a). Film thickness increases

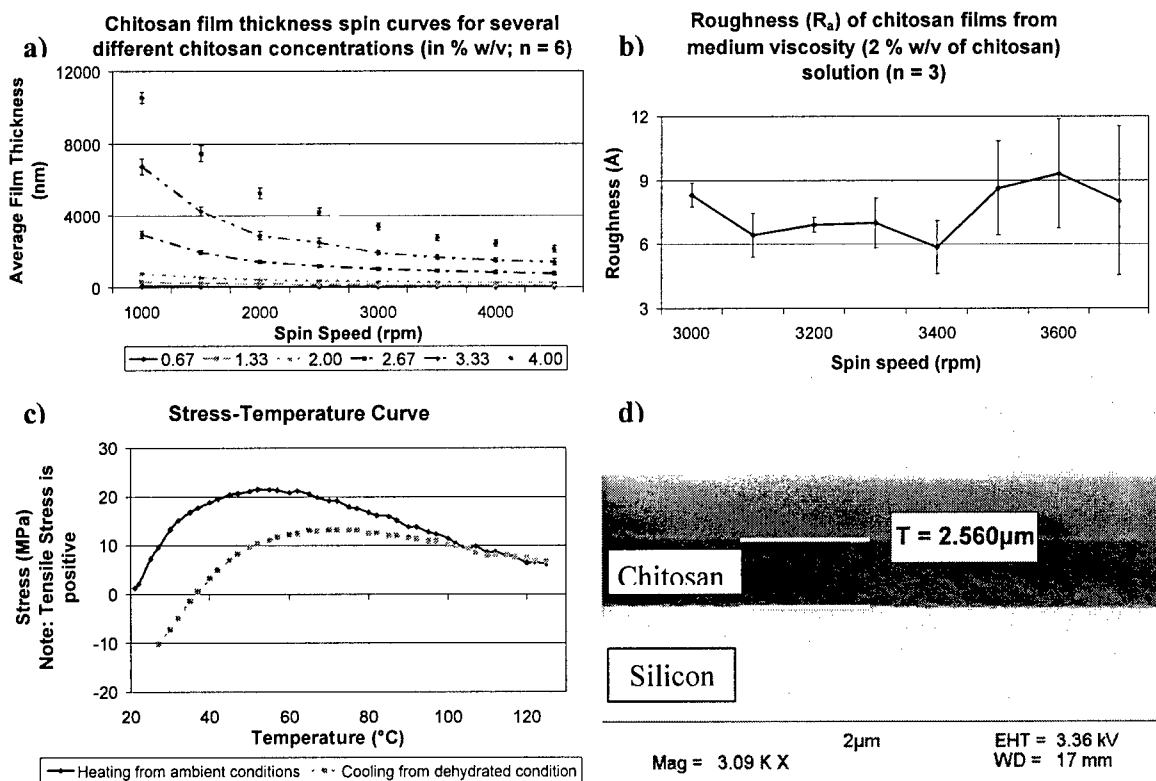


Figure 2. a) Chitosan hydrogel spin curves for chitosan concentrations varying between 1 g (0.66% w/v) to 6 g (4.0% w/v) dissolved b). Surface roughness (R_a – center-line roughness) of 3 g (2.0% w/v) chitosan films between spun using spin speeds between 3000 – 4000 rpm. c). Stress-temperature curve for 6 g (4.0% w/v) chitosan film ($T = 3.4 \mu\text{m}$) d). SEM image of a cross section of a 2.56 μm chitosan film on silicon with native oxide taken with sample at 80 $^{\circ}$ tilt.

quadratically with increasing chitosan concentration. A large range of film thicknesses can be achieved; however, the most uniform films are achieved with spin speeds between 2,500-3,500 rpm. The surface roughness of 2.0% w/v chitosan film is near 1 nm for spin speeds between 3,000–3,700 rpm. Therefore the films show good local uniformity while general uniformity across the wafer was generally better than 20%. For the smoothest films spun near 3,000 rpm, the general uniformity was 10% or better. A cross section of the chitosan film is shown in Figure 2d).

Stress in the film is an important issue, especially for applications such as IR sensing when using the material as the transduction layer. The IR-stress transduction mechanism is also used by the jewel beetle to sense IR. The stress was measured using the KLA-Tencor Flexus

FLX-2320 Thin-Film Stress Measurement System. The Flexus uses an optically-based measurement system utilizing one of two lasers – 670 and 750 nm. For intrinsic stress of the chitosan layer, a bare silicon wafer was first measured by the Flexus. This allowed the system to correct for the initial wafer curvature. The same wafer was measured again in the Flexus once the chitosan film was deposited. Chitosan has a maximum modulus less than 25 MPa, as shown in Figure 2c), while silicon has a modulus between 3-4 orders of magnitude higher.

All intrinsic stresses were measured at a temperature of 21°C. The stresses were measured for several spin-cast films deposited from 4.0% w/v chitosan solution. Due to the optical measurement system, the film was required to be reflective and of high uniformity. Therefore, only 4 of the most uniform, spin-cast films from the solution mentioned were measured. In addition, due to the film's absorption of infrared radiation from the 750 nm laser, the system needed to be manually set to use the 670 nm laser only. The absorption of infrared caused the film stress to continuously increase with repeated measurements.

The hydrogel nature of the chitosan film results in the film having the tendency to absorb ambient moisture in the environment. Accordingly, moisture in the ambient environment in the microlab is highly dependant on the temperature as the ambient conditions in the microlab are usually moderately controlled for better process control. Figure 2c) shows the stress-temperature curve for a 3.4 μm thick chitosan film. The temperature was cycled between 21°C to 125°C. Since the film started from ambient conditions (rather than a totally dehydrated form), it can be seen that the film's intrinsic stress is relatively low. The stress increases in the film due to both a loss of moisture content and thermal expansion. However, during the cooling cycle, it is seen that the stress-temperature curve forms a hysteresis curve. Measurement of the same film after stabilization in ambient conditions for several hours resulted in the same stress-temperature

curve. Therefore the loss of moisture is the likely reason behind the hysteresis aspect of the curve. Instead of the stress just increasing or decreasing with an increase in temperature, a maximum stress is achieved near 50°C for a film being heated from ambient conditions and 70°C for a film being cooled from a higher temperature, dehydrated state. It is likely that the behavior is due to a trade-off between three film characteristics which vary with temperature: thermal expansion, loss of moisture and conformational changes in the chemical structure of the chitosan.

Biaxial modulus and CTE measurements were obtained by measuring the stress in chitosan films at a range of temperatures on two separate types of substrates, silicon and aluminum. To extract the biaxial modulus and CTE from the stress data, an assumption is made that the film modulus and CTE are both independent of temperature. With these assumptions, the following approximation can be used:

$$\frac{\partial \sigma_f}{\partial T} = \frac{E_f}{1 - \nu_f} (\alpha_s - \alpha_f) \quad (2)$$

where σ_f is the stress of the film, T is the temperature of the film, E_f the Young's modulus of the film, ν_f the film's Poisson's ratio, α_s the CTE of the substrate and α_f the CTE of the film. The

biaxial modulus of the film is $\frac{E_f}{1 - \nu_f}$. By determining the slopes of the stress-temperature curves

for chitosan films on the different substrates and interpolating between the data, both the biaxial modulus and CTE of the film can be determined. The CTE for a dehydrated chitosan film was determined to be 26.566 ppm/K while the biaxial modulus was 6.371 GPa. Assuming the Poisson's ratio to be 0.45 like other polysaccharides and most resins, the Young's modulus was determined to be 3.504 GPa. This is relatively similar to the Young's modulus recorded by Domard & Domard of 3.62 GPa during their stress tests of dehydrated, mold-casted chitosan gels⁴. For films initially stabilized at ambient conditions for humidity (therefore the films

contain some moisture content), the CTE was 45.433 ppm/K, biaxial modulus 248.7 MPa and the Young's modulus 136.8 MPa (assuming a Poisson's ratio of 0.45).

It is important to note that the above measurements are sensitive to the ramping procedure used to obtain them. A ramp of 1.7°C/min was used for these measurements. This was the fastest ramp that could be used while ensuring that the substrate and temperature both stabilized for the measurement. While the hope was that the film would retain a steady amount of moisture at the set temperature when starting from a stabilized ambient condition, this is unlikely to be the case as moisture is more likely to be evaporated from the films, especially at higher temperatures even if the reading doesn't take an extended period of time. This would result in an artificial increase in stress with each measurement so the second set of CTE and biaxial modulus measurements are likely to be under and overestimations respectively for a film at ambient conditions. However, they do provide a rough estimate for simulations of devices made from the material in ambient conditions.

Chitosan Fabrication

Preparation and Purification

Medium molecular weight and high molecular weight chitosan was purchased from Sigma, St. Louis, MO. The high molecular weight chitosan (from crab shells) had 83.1% deacetylation and a viscosity of 1,700 cps (in 1% acetic acid). Glacial acetic acid (99.7% concentrated) was obtained from EMD Chemicals, Darmstadt, Germany. The 99.7% glacial acetic acid is diluted in DI water until the solution reaches a pH of approximately 4.5. Solution concentrations of 3-5% w/v are typically used. Alternatively, chitosan may be added to solvent (dilute acetic acid) until the solution is saturated. The solution is vigorously agitated to dissolve

the chitosan flakes, and then passed through a 40 μm syringe filter in order to remove large particles.

Electrodeposition

Electrodeposition offers a simplified, but restrictive, fabrication process. Chitosan electrodeposition has previously been explored by the Ghodssi group at the University of Maryland⁵⁻⁷. Patterning is determined by the traces created with a thin film Au electrode, using conventional fabrication techniques. The gold electrode is negatively biased to draw the chitosan (with a net positive charge due to the amine groups) out of solution. While electrodeposition allows the deposition and patterning of chitosan, there are many limitations that restrict its use. First, the use of a metal layer poses many restrictions in microfabrication. One example is the lowering of the thermal budget, which decreases the possible materials and deposition processes that may be used in subsequent steps. Another significant challenge is the biasing of the metal traces. If a single DC bias is to be applied across the Au surface, then there may be no islands of Au, as each trace must be biased. As a result, the entire Au pattern must be interconnected. In addition, chitosan tends to deposit beyond the edges of the Au electrode, due to field lines emerging in all directions, thus increasing the area over which chitosan is deposited. This is a drawback for devices that require precise control of feature size. Lastly, the electrodeposition process is self-insulating; as the chitosan layer thicknesses increases, it insulates the Au electrode, slowing further deposition. This ultimately causes the deposition to become self-limiting.

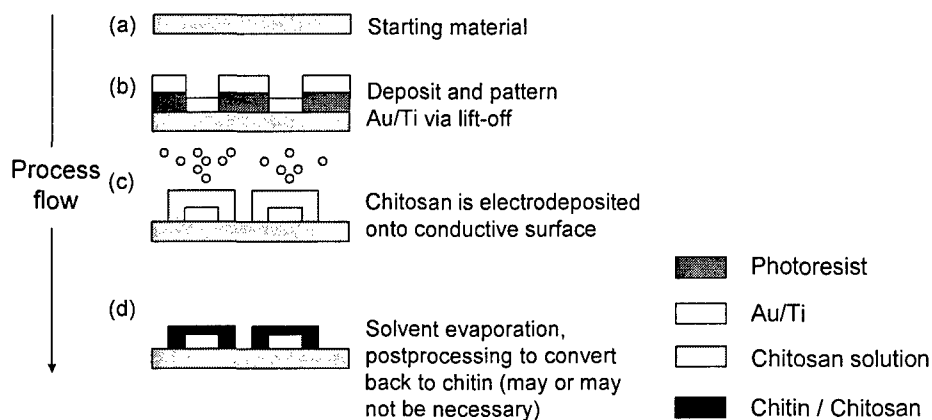


Figure 3: Chitosan electrodeposition process. The Au electrode is negatively biased, which raises the pH at the surface and causes chitosan to deposit out of solution.

A Si wafer with patterned Au electrodes is immersed in the chitosan solution. When placed in an acidic solution with a potential difference applied across two electrodes, the current flowing through the electrolyte raises the pH at the cathode, allowing chitosan to be removed from solution and electrodeposited onto a surface. A power supply providing voltages between 2 and 6 volts is applied between the electrodes. Varying the voltage allows control over plating time. A minimum of 2 V is necessary to initiate the reaction. Excessively high voltages will create a high current density that will degrade the chitosan layer. The cathode is attached to Au layer on the Si wafer and the anode is attached to aluminum or Au foil. As expected, deposition of chitosan was observed to take place at the cathode. Following electrodeposition, the wafer is washed with deionized water and gently heated at 80°C until dry. Figure 4 shows a 30 nm layer of chitosan which was electrodeposited onto a 100 nm thick gold film.

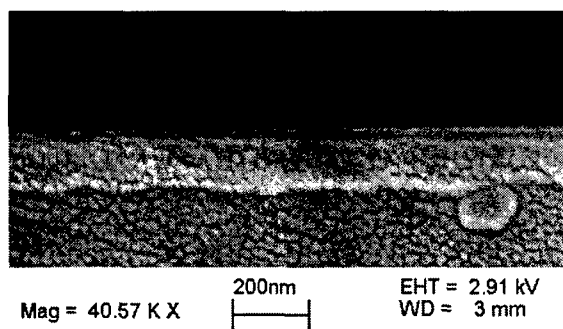


Figure 4: SEM showing 30 nm of chitosan electrodeposited onto a 100 nm Au layer on a silicon wafer.

Chitosan Photolithography

Photolithographic patterning of chitosan is more complex than electrodeposition but offers greater process flexibility and integration with semiconductor materials. To our knowledge, there has been no prior work on the development of a photolithographic patterning process for chitosan. We investigated the compatibility of chitosan with traditional photolithographic patterning processes. Figure 5 shows the traditional lithography process.

The photolithography process requires a variety of steps to produce a spatially selective, layer-by-layer removal of material. The three required removal steps are photoresist development, chitosan etching, and photoresist stripping. Because chitosan is chemically resistant, it is inherently difficult to etch. However, because chitosan is soluble in dilute acidic solutions, we determined that highly concentrated acetic acid may be used as a wet etchant. Oxygen plasma has been found to be a suitable dry etchant. The final step in pattern transfer is photoresist stripping.

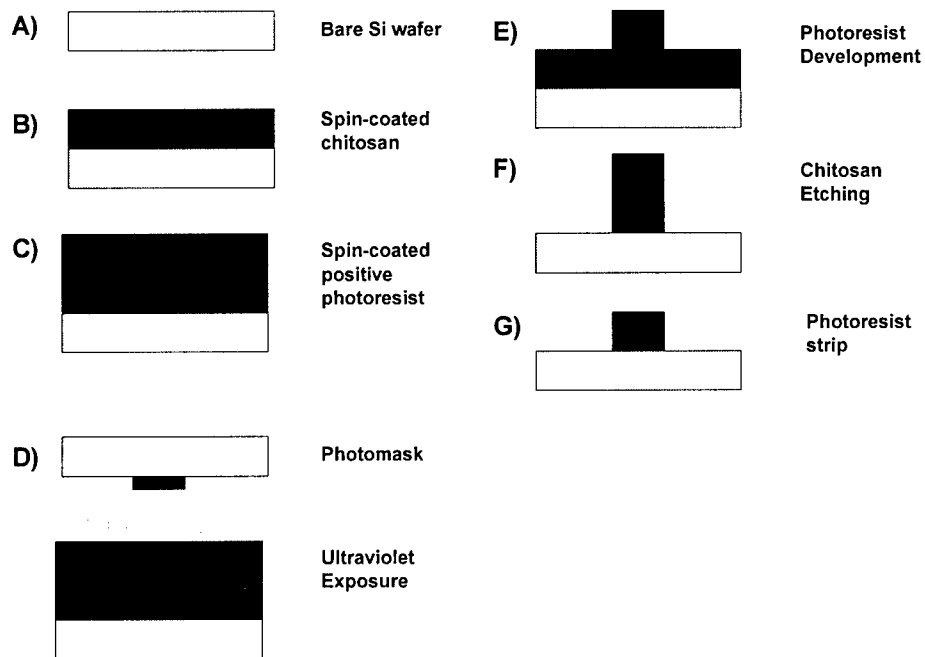


Figure 5: Conventional photolithographic patterning process for chitosan. Photoresist stripping step requires some modification.

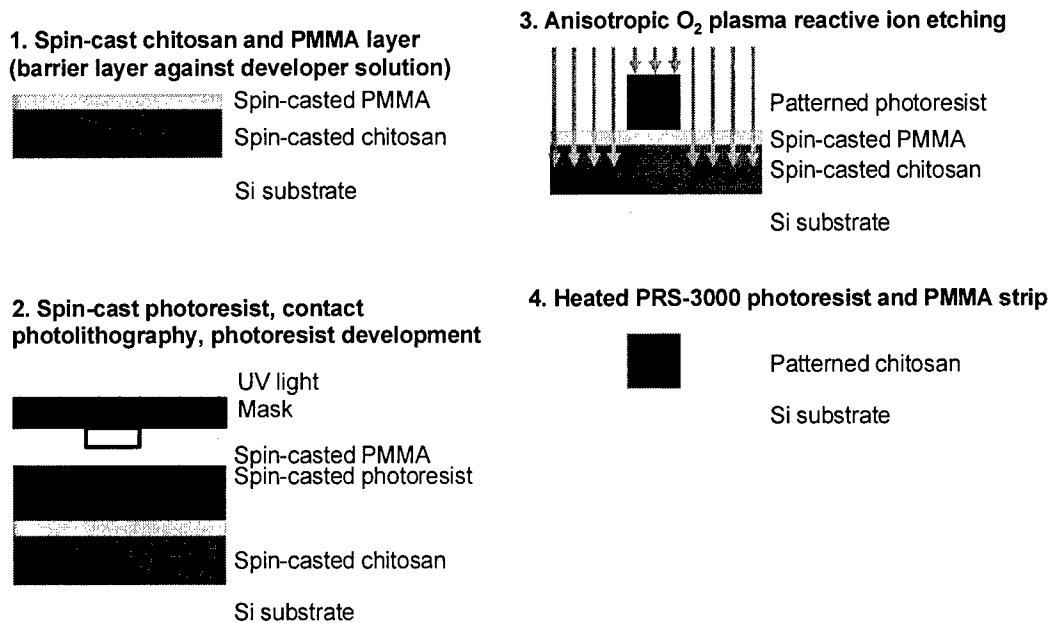


Figure 6: Modification of photolithography process with PMMA protective layer to allow photoresist stripping.

The following sections detail the results obtained along each step of the lithography process. Figure 6 shows the primary modification made to the conventional process – a PMMA (polymethyl methacrylate) barrier layer which may be used to avoid certain difficulties with

various chemicals used in the lithography process. In addition, problems such as film cracking and difficulty with wet etching are discussed and overcome.

Spin-casting

Spin-casting is the conventional method for depositing photoresists during the lithography process, and has also been found to be a suitable means for depositing thin films of chitosan onto the surface of a silicon wafer. A small amount of liquid solution is dispensed onto the surface of the wafer, which is then spun at a high speed to evenly coat the wafer with the dispensed solution. Following chitosan spinning, the wafer is heated at 80-120°C for solvent evaporation. Film thickness can be controlled by the spin speed and spin time, and is also affected by the viscosity of the liquid.

A layer of photoresist is deposited via spin-coating at 4,000-5,000 rpm for 60 seconds. For a positive resist photolithographic process, the wafer may be coated with OCG 825 (G-line / 436 nm) photoresist or OiR 10i (I-line / 365 nm) photoresist. Choice of resist depends on the exposure lamp used and existing, optimal thickness recipes for the resist. We have found Shipley OiR I-line resist to produce fewer nonuniformities and to be more compatible with chitosan than Shipley OCG-825 G-line photoresist. For thicker resists (approximately 10 microns thick), SPR-220 may be spun at 1,800 rpm. Following photoresist deposition, the resist is exposed to UV light through a photomask using a Karl Suss MA6 mask aligner compatible with both G-line and I-line resists.

Compatibility with Resists

Because both photoresist and chitosan are organic compounds, and chitosan had not been previously used in a semiconductor fabrication process, it was initially unclear whether there would be deleterious chemical interactions that would prevent the layering and exposure

processes necessary for photolithographic development. Our work has shown that using photoresists over chitosan layers requires certain modifications to the conventional lithography process.

An initial test was performed to verify the existence of two distinct layers (a chitosan layer and a photoresist layer) on the silicon substrate. SEM imaging was used to verify that the photoresist layer would not mix with the chitosan layer. Figure 8 shows an SEM cross-section that shows a distinct 1.1 μm thick layer of G-line photoresist on a 310 nm thick layer of chitosan.

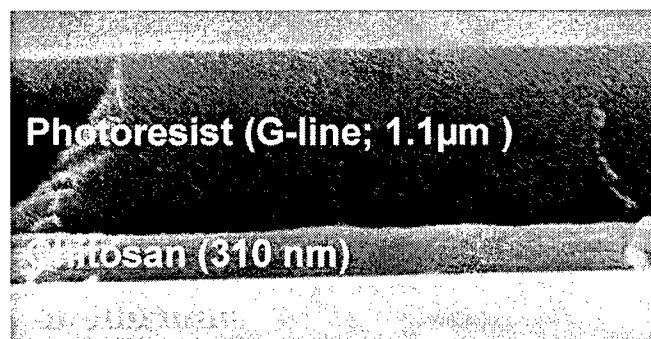


Figure 7: SEM showing 1.1 μm photoresist layer coated over 310 nm chitosan. The distinctness of the layers is clearly evident.

Several imperfections became apparent during the photolithographic process. One imperfection that occurs in various places across the wafer is the “crop circle” or indentation / pit (Figure 8, left) which is due to localized areas of stress in the film after development of the photoresist. They mainly occur due to swelling of the chitosan when developer solution seeps through pinholes resulting from non-uniformities due to foreign particles in the chitosan. The swelling increases stress in those areas resulting in the indentations. The imperfections reduce yield but are not so widespread as to prevent the successful formation of dies. These imperfections may be removed with better filtering of the solution.

Film cracking (Figure 8, right) is a second imperfection that has been found to occur. This is another imperfection mainly caused by swelling of the chitosan due to absorption of

developer in exposed areas. The problem is compounded by coating a chitosan-bearing wafer with multiple coats of photoresist, which increases the intrinsic stress in the layers allowing even minute chitosan layer swelling to crack the resist layers. This problem is solved by utilizing a thick enough barrier layer of PMMA or underexposed photoresist to prevent the developer from reaching the chitosan and thus swelling of the chitosan layer.

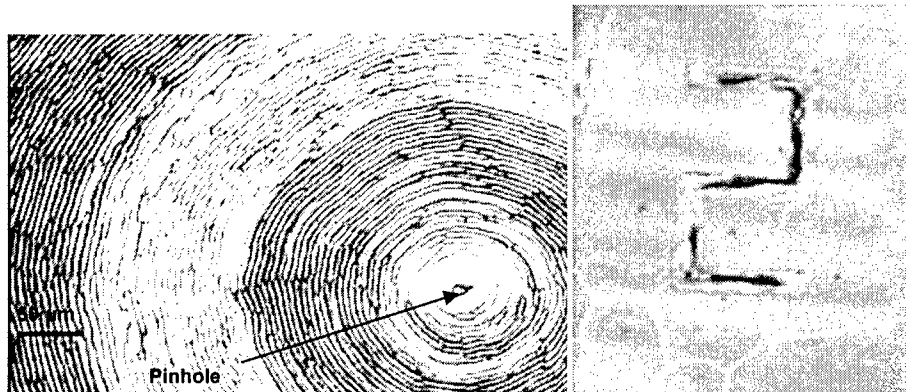


Figure 8: A) "Crop circle" imperfection due to swelling of chitosan at a pinhole in the resist caused by small particles found in the chitosan solution. B) Film cracking occurring due to swelling of the chitosan and increased intrinsic stress in multiple resist layers.

Development

For a positive resist, the development process washes away the exposed photoresist areas. Figure 9 shows positive photoresist features that successfully transferred following exposure and development.

Etching

Chitosan etching is challenging because of chitosan's inherent chemical resistance. Chitosan dissolves in acids and therefore a highly concentrated acid may serve to remove the material. However, etching requires the use of an etchant that is selective to chitosan over the masking material. O₂ plasma has been found to be a suitable dry etchant, which offers several advantages over alternative wet etching processes.

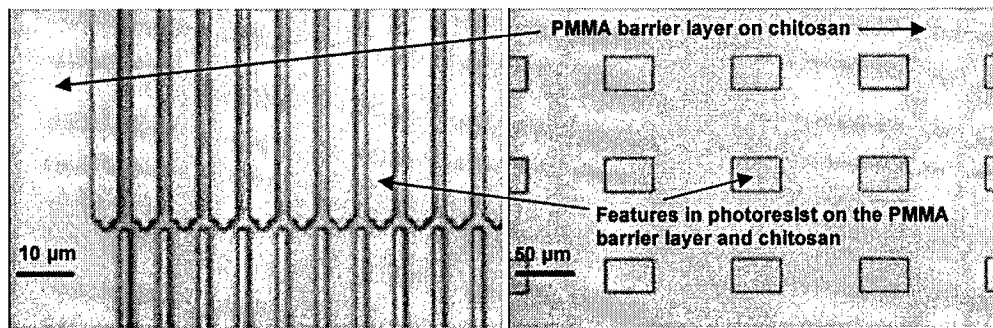


Figure 9: Patterned (post-development) photoresist masking 2 μm thick chitosan utilizing a 400 nm PMMA barrier layer and 4.0 μm (2 coats of 2.0 μm G-line) photoresist.

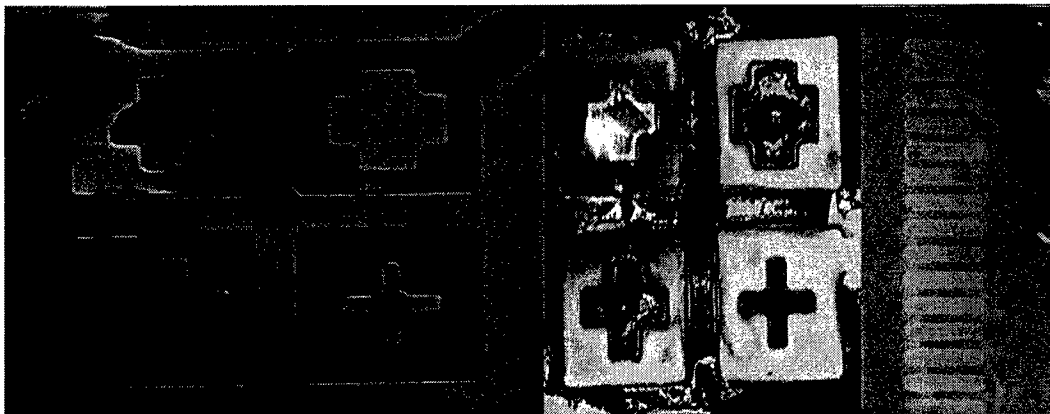


Figure 10: Left - Patterned photoresist over chitosan. Middle and Right - Features following wet etching using highly concentrated acetic acid. Wet etching has been observed to lack uniformity and control compared to alternative dry etching.

Wet Etching

Wet etching using highly concentrated acetic acid was initially attempted, but the selectivity between the masking and chitosan layers and the chemical interaction between chitosan and photoresist with the acetic acid etchant has shown wet etching to be suboptimal.

Figure 10 shows features defined in photoresist before and after etching. The patterns shown on the left are somewhat distorted because this wafer was our first attempt at photolithographic patterning of chitosan. The middle image in Figure 10 shows the harsh effect the highly concentrated acetic acid has on the chitosan and photoresist layers. High resolution features are difficult to obtain with wet etching because of the harsh treatment and lack of selectivity.

Dry Etching

Dry etching is the preferred means of material removal due to its anisotropy and improved uniformity and control. Dry etching is generally preferred over wet etching because there are fewer disposal problems, less undercutting of photoresist features, and better critical dimension control⁸. Chitosan may be dry etched using oxygen (O₂) plasma, either in a plasma etcher or a reactive ion etcher, such as the Plasma-Therm PK-12 Reactive-Ion Etcher system. Oxygen plasma vaporizes organic materials making it a good etchant for chitosan. However, since photoresist is an organic compound, the reactive ion etch will also etch the photoresist mask. The etch rate of chitosan is greater than the photoresist etch rate, providing some selectivity during etching. The photoresist thickness can also be made thick enough and patterns wide enough to account for etch erosion.

The etch rate of both photoresist and chitosan in the oxygen plasma reactive ion etcher was determined by calculating the difference between the step heights of a pattern of the material on a silicon wafer, before and after etching, using the AS200 surface profiler. The result showed that at an oxygen flow rate of 50 sccm and RF power of 70 W, the etch rate of photoresist (both G-line and SPR-220) was approximately 200 nm/min. At the same flow rate, but RF power of 100W, the photoresist etch rate was approximately 280 nm/min. At an RF power of 70W and an oxygen plasma flow rate of 50 sccm, the etch selectivity is 1.65:1 for chitosan (330 nm/min) to photoresist (200 nm/min).

A Technics-C PE-IIA plasma etcher was used for O₂ plasma etching of chitosan. With RF power of 50 W and an O₂ flow rate of 50 sccm, the chitosan etch rate was found to be 210 nm/min for an etch selectivity (chitosan to photoresist) of 1.37:1. The chitosan etch rate was determined by measuring step height profiles for several etch times using an Alpha-Step IQ

Surface Profiler from KLA-Tencor. Step heights were measured following isotropic dry etching in a Technics PE-IIA plasma etcher. A chitosan-coated wafer with an initial pattern of 2 μm thick OCG 825 G-line photoresist was etched with 50 sccm O_2 plasma and 50 W RF power. As a control, a 2 μm layer of OCG 825 G-line photoresist on bare Si was also etched under the same parameters as the chitosan wafer. The O_2 plasma etches both the chitosan and the photoresist, albeit at different rates. The photoresist etch rate was determined solely by measuring the step height of the control at various times, taking the difference and dividing by the etch time. The chitosan etch was determined by measuring the chitosan-photoresist profile at multiple times, defining the first step height as the initial height of the photoresist. The amount of etched chitosan was determined by taking the total step height and subtracting the photoresist thickness, which is the initially measured step height corrected with the photoresist etch time.

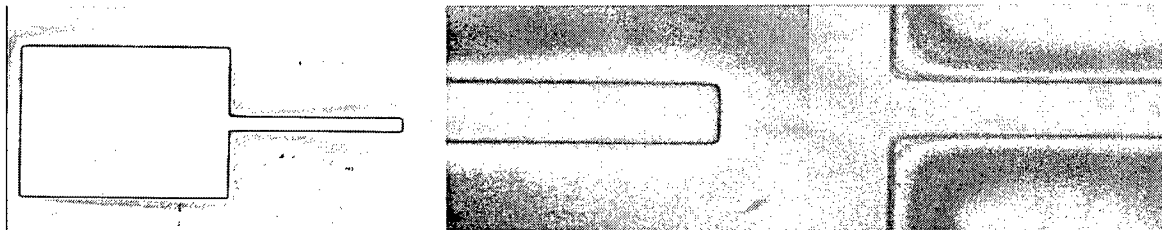


Figure 11: O_2 plasma etching of chitosan in a Technics-C plasma etcher after 7 minutes at 50 W RF power and 50 sccm O_2 plasma. The blue-purple color is chitosan that has not yet been fully etched. The isotropic nature of the plasma etch is evident by the coloration in the right-most figure.

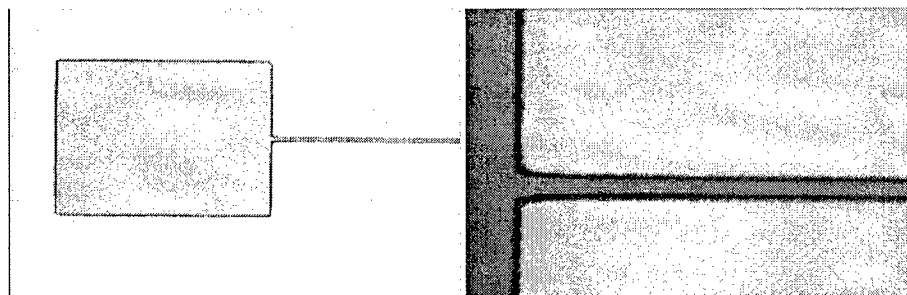


Figure 12: O_2 plasma etching of chitosan in a Technics-C plasma etcher after 8 minutes at 50 W RF power and 50 sccm O_2 plasma. The chitosan is fully etched.

Photoresist Stripping

The photoresist stripping step was found to not work when following conventional lithography processes, especially wet processes. The addition of a barrier layer, such as PMMA, between the chitosan and the resist was found to be necessary to allow the resist strip to go forward. In this experiment, we attempted to strip the photoresist without ever etching the chitosan – hence all features should be removed following this process. The wafer was placed in

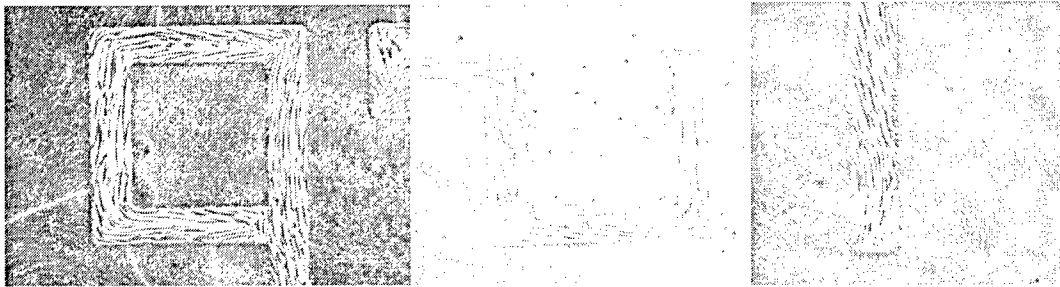


Figure 13: Difficulty in stripping the photoresist following development. A) After 5 minutes in PRS-3000. B) After 24 hours in PRS-3000. C) After 5 minutes in acetone.

PRS-3000 photoresist stripper for periods of 5 minutes and 24 hours without observing the expected removal of the photoresist. Placing the wafer in acetone also did not remove the hardened photoresist. Features remain after all three cases as shown in Figure 13. This is likely due to chemical interactions at the photoresist-chitosan interface when exposed to developer solution, which compounded with the chitosan swelling resulted the images in Figure 13. The concentrated acetic acid etch used in the wet etch process may also affect the interface, though its effect is likely much less than the developer solution. The results from proper photoresist stripping and thus well-patterned chitosan features are shown in Figure 14.

Feature Size

One area of primary concern is the minimum feature size that may be obtained in the photolithographic process. A great number of variables affect the minimum feature size such as the materials, wavelength of exposure source, and the etching selectivity and degree of anisotropy. The exposure source – i.e. the use of G-line or I-line, introduces a diffraction

limitation into the lithography process. In the best case, the minimum feature size is approximately the wavelength of light, which for G-line is 436 nm and for I-line is 365 nm. Equipment limitations such as the minimum gap size in contact printing and mask alignment normally limit feature sizes to 1-2 μm . Projection printing can be used to approach the minimum feature sizes which the resists can be used for, however diffraction losses limit the complexity of the features. For infrared sensors, the minimum linewidth may be as generous as 20 μm , due to the diffraction limit for these longer wavelengths. For microelectromechanical systems, a minimum feature size of 1-2 μm is often sufficient.

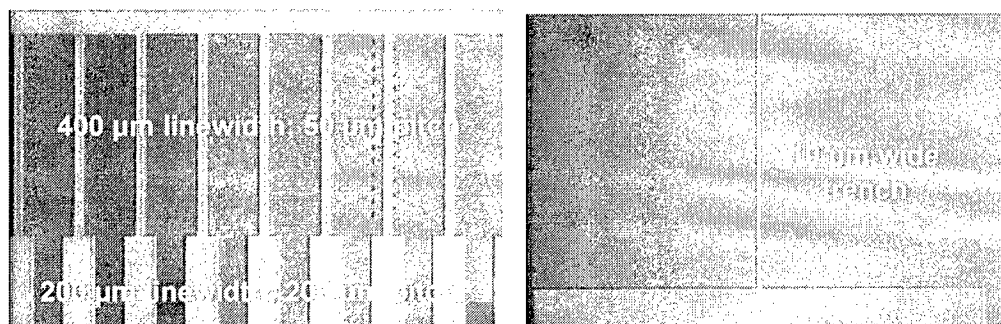


Figure 14: Chitosan features down to 10 μm following photolithographic patterning.

Figure 14 shows a successful photolithographic pattern transfer – including chitosan etching and photoresist stripping. We have achieved feature sizes down to $\sim 4 \mu\text{m}$. Photolithographic patterning of chitosan offers a microfabrication and MEMS compatible batch process with great feature control and potential for process integration.

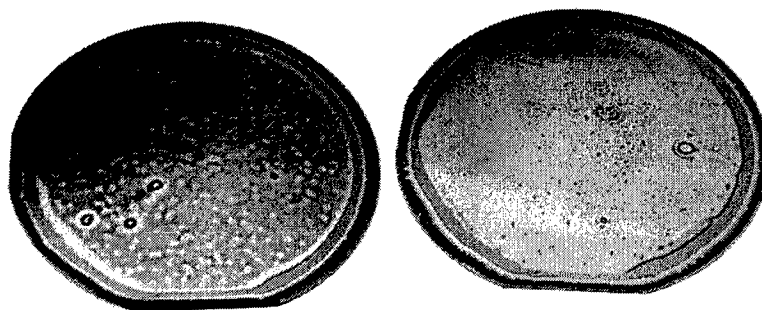
Post-processing

All of the experiments discussed thus far have used chitosan rather than chitin. It remains unclear whether chitin offers a significant benefit over chitosan, as the primary difference between the two is the percentage acetylation and the presence of infrared absorption peaks in chitin in the 6-7 μm band that are not found in chitosan. The use of chitin rather than chitosan

may be advantageous because it: 1) is the naturally occurring polysaccharide found in the jewel beetle, 2) possesses increased thermal stability, and 3) has increased strength. However, we have identified a means of converting chitosan to chitin following deposition of chitosan onto a silicon wafer, thus allowing us to work with either material.

Because chitin is insoluble in most commonly available solvents, it is advantageous to form solutions of the more processing-friendly chitosan for thin-film deposition, and then acetylate the chitosan back to chitin. Chitosan films may be converted to chitin films by N-acetylation, following the method of East and Qin, using 5% v/v acetic anhydride in methanol⁹. Following the ratio of East and Qin, 10 mL of acetic anhydride/methanol solution is used for every 12.9 mg of chitosan fibers. To prevent O-acetylation, 1 M NaOH was applied. Following acetylation, the wafer is rinsed using DI water.

Figure 15 shows the wafers and FTIR absorption spectrums before and after chitosan acetylation. Chitosan has a distinct purple color when deposited onto a wafer, which becomes a yellowish color after the acetylation process. The FTIR absorption plots are similar, with the exception of pronounced peaks in the chitin FTIR over the 6-7 μm wavelengths.



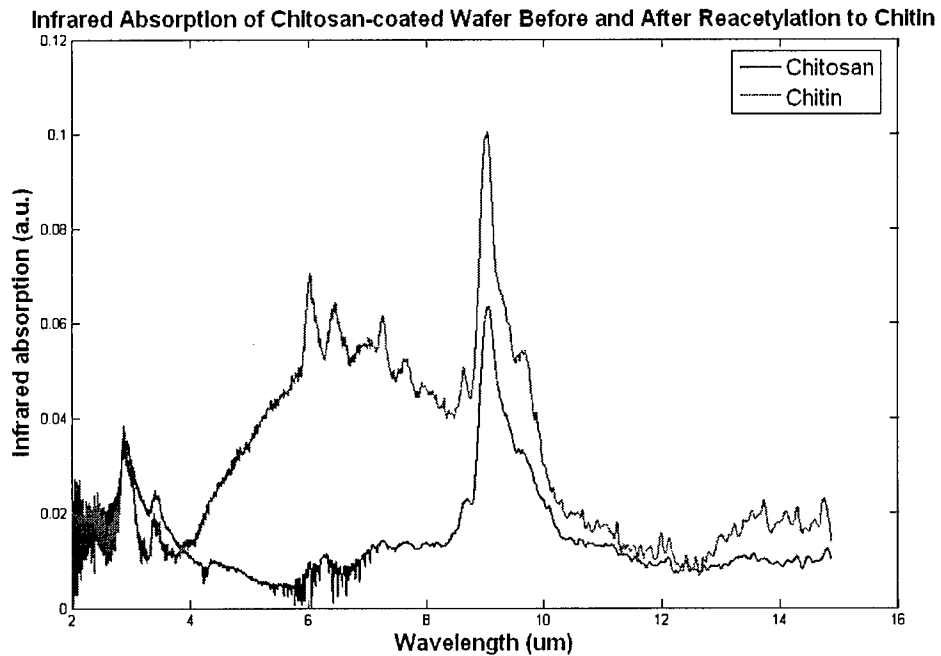
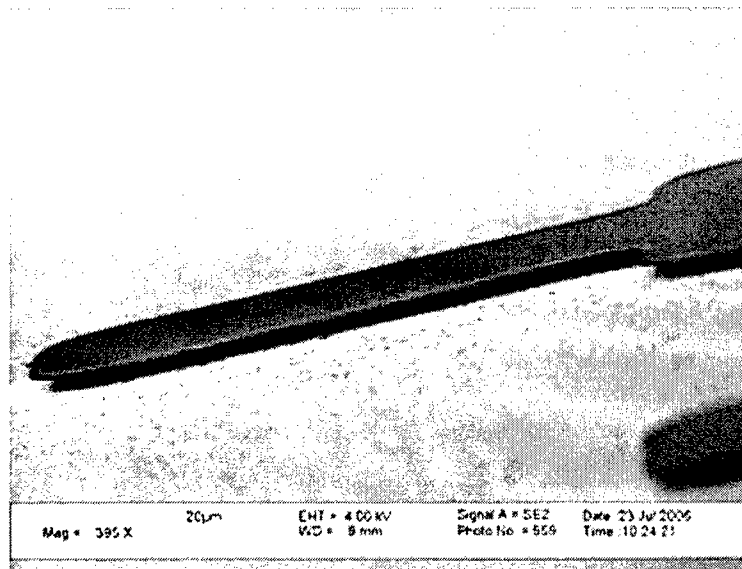


Figure 15: Chitosan before (top left) and after (top right, now chitin) the acetylation process. FTIR spectroscopy confirms that chitosan has been converted to chitin.

Device Processing

Device #1: Photomechanical Thin-Film Transistor

Figure 16 shows a cantilever beam composed entirely of chitosan. The beam was defined using the photolithography process and then the bulk Si was etched / undercut using an isotropic XeF_2 etch to release the structure. FTIR was used to verify that the XeF_2 etch did not affect the chitosan features.



Chitosan After XeF₂ Release

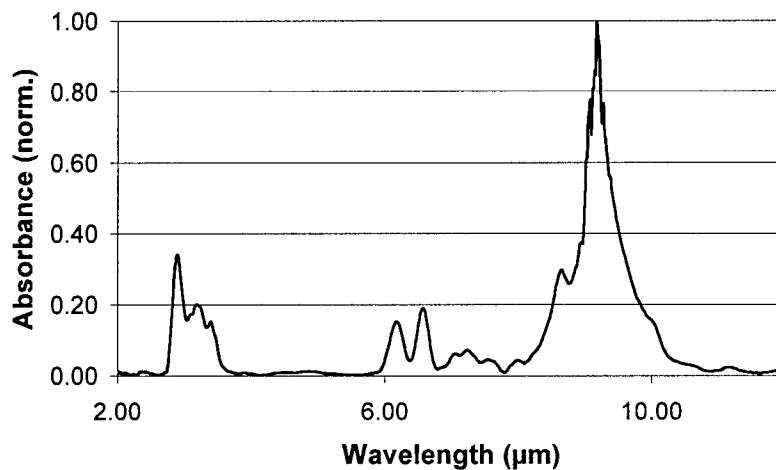


Figure 16: Cantilever beam composed entirely of chitosan. Chitosan serves as a sufficient structural material to support itself. Another layer with thermal mismatch is required to make use of the bimorph effect. FTIR shows that chemical structure of chitosan feature underwent little to no change when exposed to XeF₂ etch.

The Photomechanical Thin-Film Transistor – PTFT – is an imaging pixel based on a back-gated TFT structure. The proposed structure would incorporate chitin/chitosan on top of the channel of the transistor and/or replace the dielectric. One version of the PTFT structure is shown in Figure 1a) and its proposed fabrication sequence in Figure 1b). A back-gated TFT is utilized as the base structure because of four main reasons:

1. Allows chitin/chitosan to be deposited directly above the transistor channel and as the final layer prevent thermal budget issues.
2. The reflective, metal gate would result in unabsorbed IR to be reflected back through the chitin/chitosan layers for additional absorption.
3. TFTs are readily scalable and arrayable minimizing size and interconnect issues.
4. TFTs can be built on flexible substrates and can be fabricated utilizing low thermal budget processes making it more compatible with biomaterials.

Such a device can be envisioned to be built into a staring IR imaging array similar to a TFT monitor or even incorporated into a TFT monitor expanding its usage into both a display and imaging sensor simultaneously.

Current work on this concept is occurring in two main areas: simulation and a MOSFET-based prototype.

Simulation of a stressed thin-film transistor

The focus of this work is to develop a design model for the development of a photomechanically strained TFT array for the detection of IR radiation. The research approach that will be used here is:

1. Effectively model the baseline electrical characteristics of a TFT,
2. Subject this baseline TFT to a stress/strain field and observe the effect of stress on the electrical characteristics (mobility),
3. Modify the simulated TFT design to include a conformally coated layer on these TFT devices.

The layer is an electrically insulating, light absorbing layer of known properties, and the effect of variable thickness of this layer on the electrical properties will be parametrically observed.

- Import the properties of chitosan into the model developed in (3) to determine the effect of light intensity, through photomechanical stress in the chitosan layers on top of the TFT devices. Again, the thickness of this layer will be parametrically studied and the effect on electrical characteristics will be characterized.

Coupled stress/strain modeling with electrical simulation of TFTs is rarely performed today due to the complexity of the problem and the lack of suitable simulators for the task. From published research in literature and solid-state theory, it is known that when a stress is applied to a classic thin film transistor (TFT), there is a change in electron and hole mobility. In order to see the influence of stress, two widely used commercial software simulation tools, Tsuprem4 and MEDICI, are being used for simulation of PTFT designs. Tsuprem4 is a process simulator that can be used to construct a rough approximation of a TFT device. MEDICI is a device simulator used to simulate the electrical characteristics of the device including I-V curves and plots of mobility. While neither tool can accurately model TFT devices without manual input of material properties including grain size for more complex materials like polysilicon, for initial approximations the tools can be used to model a bottom-gated MOSFET and see if stress input into the structure will result in mobility and thus current changes. These simulations can also be used to roughly gauge the sensitivity of a similar PTFT device. With further optimization of the

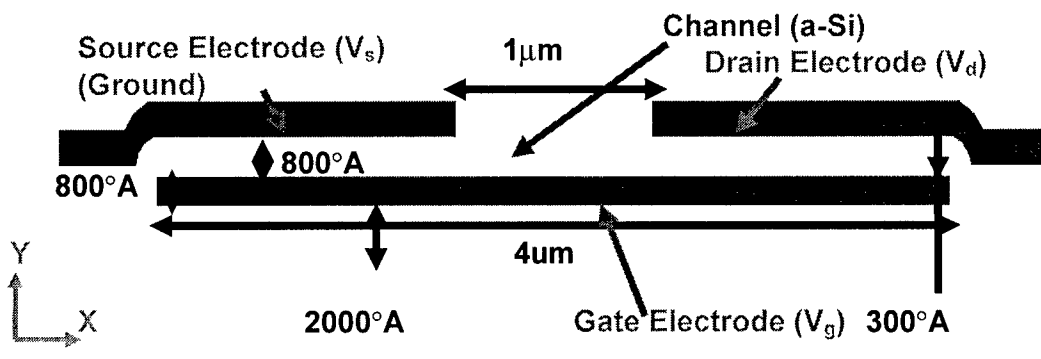


Figure 17: Sketch of the thin film transistor (TFT) to be modeled (actual model uses Si rather than a-Si).

simulation with results from the prototype devices, the simulation could be used to accurately model TFT characteristics and be used to couple MEMS stress and electrical simulation in general. From this point on, the bottom-gated MOSFET will be referred to as the “TFT device.”

In this first analysis, (1), the TFT device is developed by Tsuprem4 and then the device is exported to MEDICI to construct its IV curve. The sketch of the TFT construct with Tsuprem4 is as shown in Figure 17. In Figure 17, the yellow, dark blue, and light blue parts represent silicon, aluminum, and silicon oxide respectively. The top silicon layer is served as channel and the bottom one is substrate.

While analyzing the IV curve of the TFT, the source electrode is grounded and the drain (V_d) and gate (V_g) electrodes are at a certain voltage. Then, a current (I_{ds}) is generated and flows from the source to the drain through the channel, while gate controls the on and off state of the I_{ds} current. In order to see the response of the TFT under stress (uniform along entire device), (2) different S_{xx} stress (the stress along the channel) is applied to the device. The parametric variation of stress on the TFT results in changes in device characteristics across a wide range of stress. This baseline stress application must be considered in future designs.

If we plot the electron and hole mobility at the center of the channel against different stress, we can get a relation between the electron/hole mobility and the stress applied as shown in

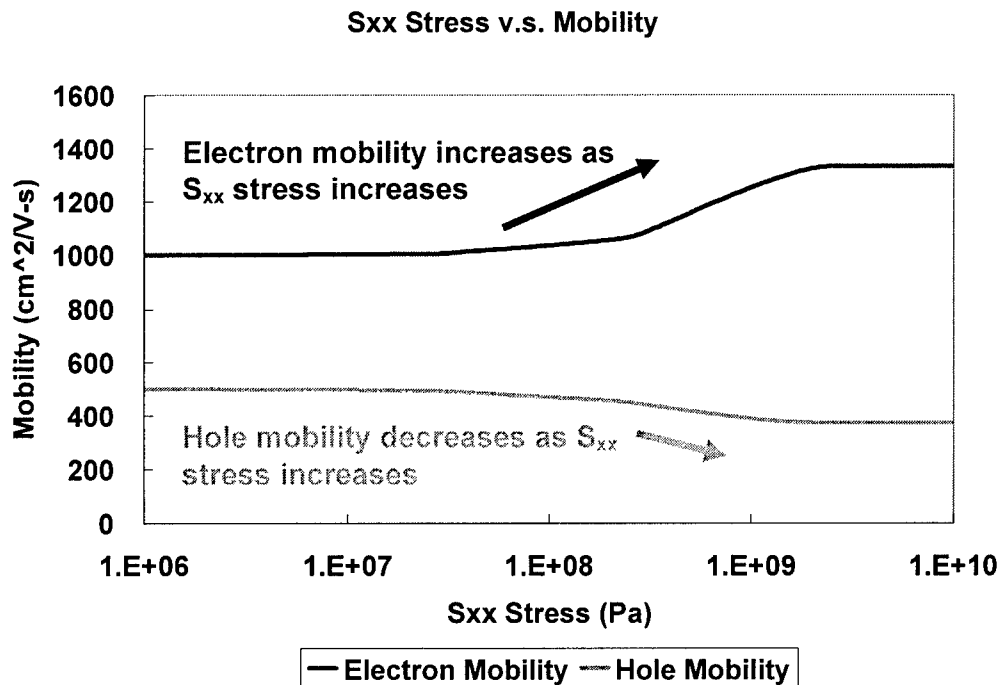


Figure 18: The electron and hole mobility at the center of the channel under varying stress.

Figure 18. In Figure 18, the electron mobility increases with S_{xx} stress but the hole mobility decreases. Figure 19 shows that I_{ds} current ($V_g = 50V$ and $V_d = 50V$) increases with stress. It is because the increase of electron mobility is much more than the decrease of hole mobility.

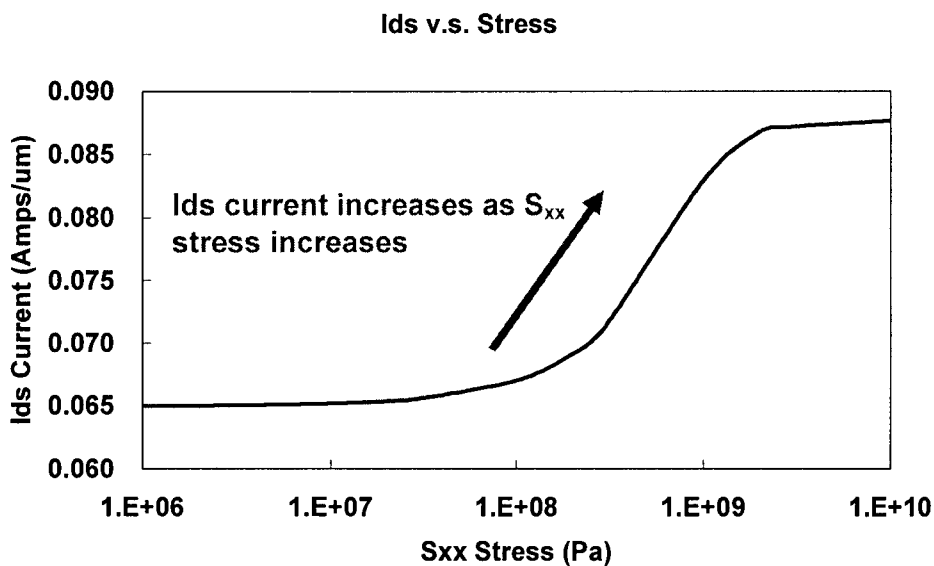


Figure 19: The I_{ds} current when V_{gs} and V_{ds} are 50 Volt

Prototype IR-sensitive Chitosan NMOS transistor

A MOSFET-based prototype was chosen due to the availability of nanogap MOSFET structures from Donovan Lee and Prof. Tsu-Jae King of the UC Berkeley Device Group. Also, the size of the structures met DARPA milestones being far smaller than the 20 x 20 μm pixel requested. The nanogap MOSFET structure is essentially a standard, bulk NMOS transistor (with polysilicon gate) where most of the SiO_2 dielectric has been removed by a hydrofluoric acid vapor etch. The nanogaps are 10 to 15 nm. The difficult task was to concentrate and fill the nanogaps with chitosan. In order to do this, several preparatory steps were first required. The first step was to immerse the chip with the structures in O_2 plasma for 1 minute to allow a native oxide to build on the surfaces of the nanogap to make the surfaces more hydrophilic. Then, the chip attached to a platinum electrode and immersed into a 2% w/v solution of medium molecular weight chitosan and 2:1 buffered acetic acid. The chip and beaker were both placed into a bell jar which was placed under 17 Hg of vacuum and left for 24 hours for degassing and to allow the solution ample time to wet and fill the gap. At this point the beaker was removed from the bell jar and the electrodeposition setup completed as in Figure 20c). Biasing the silicon substrate with a constant voltage of 3V for 30 minutes resulted in the filling of the nanogaps with chitosan as well as deposition of chitosan on all other surfaces as well. SEM images of the chitosan transistor are shown in Figure 20d) while a top down view of a chitosan transistor is shown in Figure 20e).

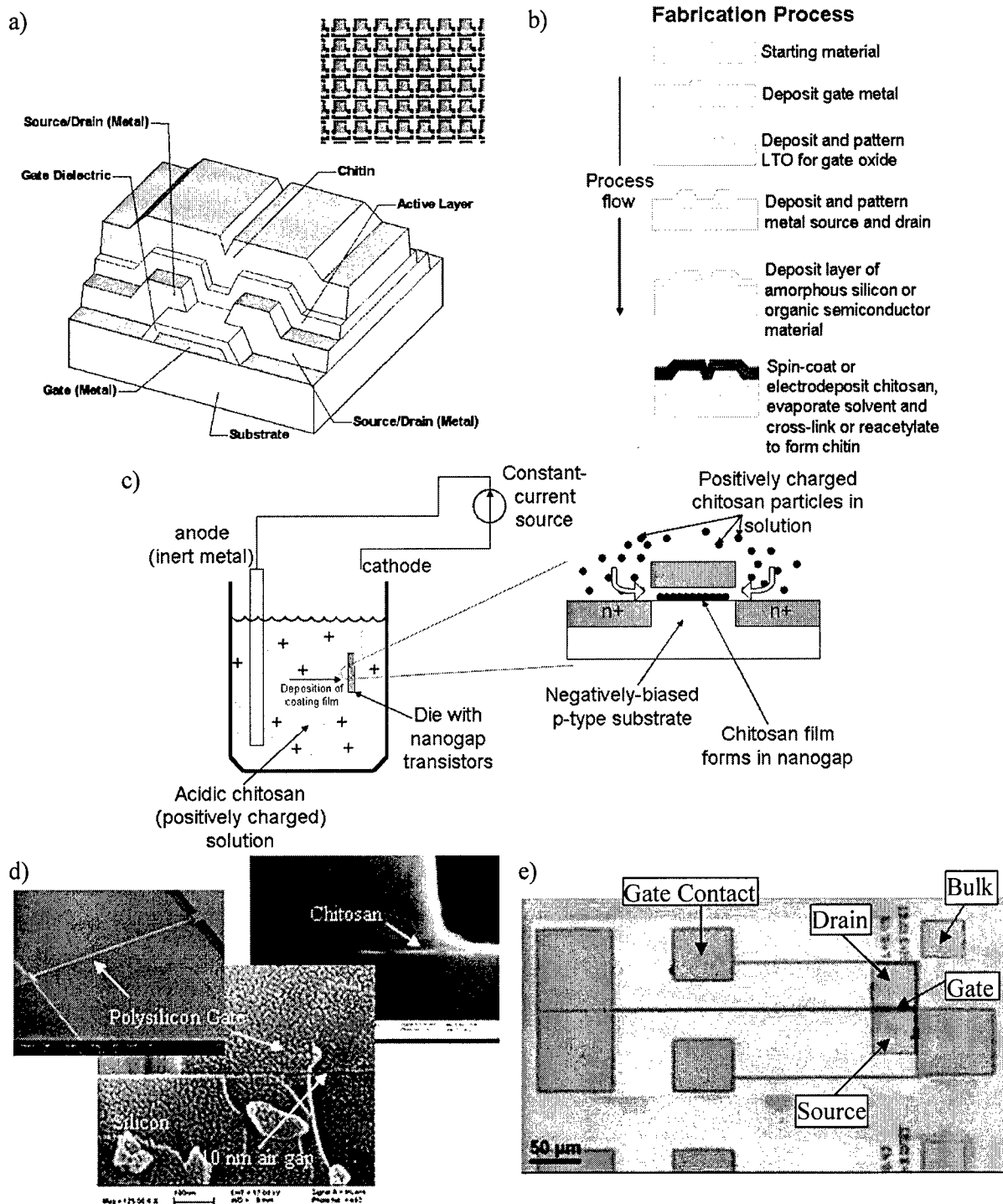


Figure 20. *a)* Photomechanical Thin-Film Transistor (PTFT) concept and array of TFTs in background *b)* One possible PTFT fabrication process. *c).* Chitosan deposition process into nanogap MOSFETS. *d).* SEM images left to right: 2 μm nanogap MOSFET transistor from the top; Cross section of nanogap MOSFET; Cross section of a chitosan-filled nanogap MOSFET. *e)* Image of a chitosan-filled nanogap MOSFET taken with 10x objective from Reichert Microscope.

Preliminary testing of the chitosan transistor structures was performed. The transistors tested had gate lengths of 1, 2 and 5 μm and widths of 5 μm . A standard microscope probe station located in a sealed isolation hood was utilized for the tests. All tests were performed on unpackaged designs. There was no metallization performed on the transistors and the probes were punched through the chitosan layer and native oxide to the n+ polysilicon and silicon contacts. The probe station setup is shown in Figure 21a). An HP4145 Semiconductor Analyzer was used to bias and record I-V curves from the test devices. The microscope illuminator was used as a rough IR source. The 3200K (color temperature) lamp was used and once the beam went through the glass lenses and silicon wafer placed between the objective lenses and device, bandpassed IR between 1.5 and 4 μm should result with a nominal peak intensity of 60 $\mu\text{W}/\text{cm}^2$ at 2 μm . This was computed based on the ideal blackbody curve of the lamp, assumption of 5 ideal glass lenses between the lamp and device and one ideal silicon wafer between the objective lenses and device.

Recorded drain current (I_d) vs. gate voltage (V_g) of the devices shown displayed distinct differences when the devices were irradiated by IR. When the light was on, the V_t (turn-on voltage) increased causing the current to decrease. For the 1 μm chitosan NMOS transistor shown in Figure 21b), the current difference for a V_g of 2V and V_d of 50 mV was about 1.75 μA . This differential current is well within normal MOSFET operating conditions as currents less than a nanoamp can still be sensed by sense amplifiers which are used in memory chips. The transistor operating characteristics were verified by plotting out all the currents, from the drain current to the body current. From the plot in Figure 21c), it is clear that the transistor is operating correctly as the source current is the inverse of the drain current and both gate and body currents are negligible. The other set of curves recorded were of the drain current (I_d) vs.

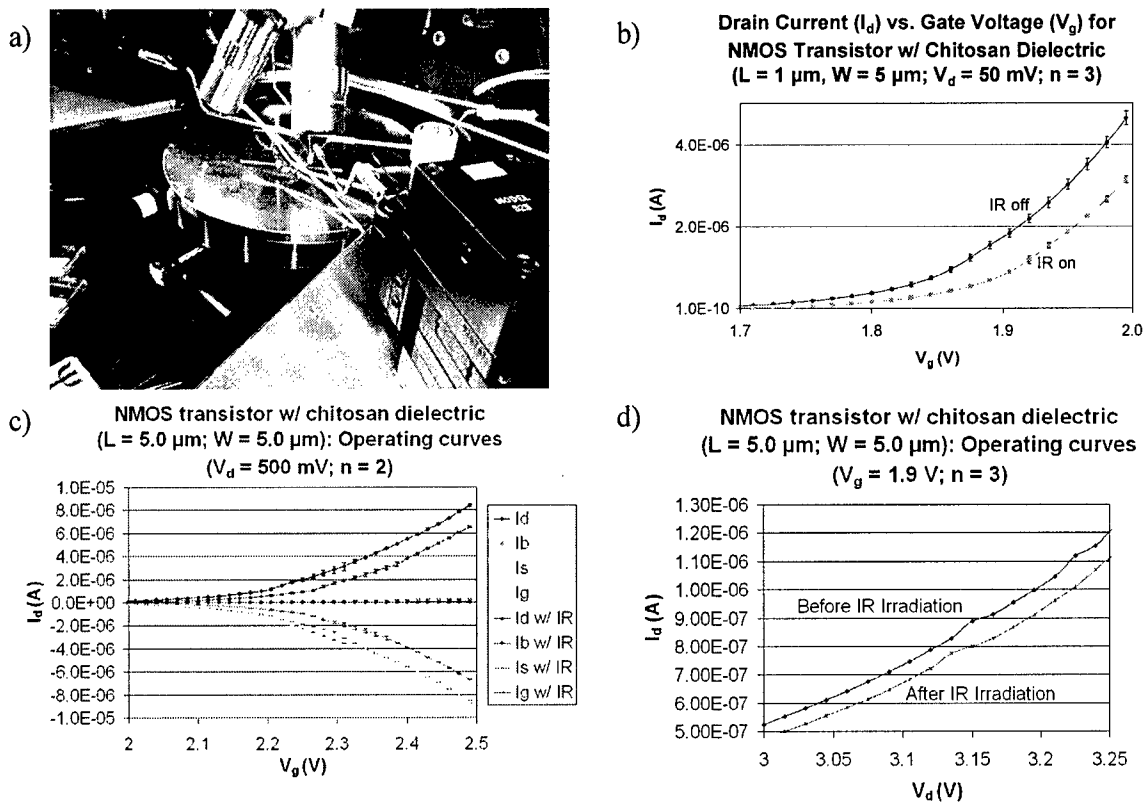


Figure 21. *a)* Probe station measurement station which is located in an isolation hood *b)* Drain current (I_d) vs Gate Voltage (V_g) operating curves for $1 \mu\text{m}$ NMOS transistor with partial chitosan dielectric irradiated by IR of nominally $60 \mu\text{W}/\text{cm}^2$ intensity and peak wavelength of $2 \mu\text{m}$. *c)* Operating curves for $5 \mu\text{m}$ NMOS transistor with partial chitosan dielectric for varying gate voltage, $V_d = 500 \text{ mV}$ and under irradiation of IR with nominally $60 \mu\text{W}/\text{cm}^2$ intensity and peak wavelength of $2 \mu\text{m}$. *d)* Operating curves for $5 \mu\text{m}$ NMOS transistor with partial chitosan dielectric for varying drain voltage, $V_g = 1.9 \text{ V}$ and under irradiation of IR with nominally $60 \mu\text{W}/\text{cm}^2$ intensity and peak wavelength of $2 \mu\text{m}$. Note that after irradiation, curve shift is permanent until gate bias is removed.

drain voltage (V_d) shown in Figure 21d). The change in current here is not as substantial and interestingly, the change is held after irradiation, even if the IR source is turned off. We are theorizing that this may be due to the constant gate bias which could be holding any conformal changes in the chitosan dielectric and thus keeping the current from returning back to the original “IR off” state. This may prove to be advantageous though for an IR-based memory device.

Future work on the chitosan MOSFETs will focus on optimizing the transistor structure parameters for increased sensitivity. These parameters include gate thickness, width, length, ratio of chitosan to SiO_2 dielectric and dielectric thickness. We are also working on integrating these devices with the appropriate die handling such that the standard detectivity, D^* , can be

appropriately quantified. Based on the results of the chitosan MOSFETs, the proposed fabrication processes of the PTFT will be revised. Further simulation for the PTFT is to be performed and will help toward optimizing the PTFT structure.

Device #2: Chitosan-coated MEMS Strain Gauge

Based upon our current understanding of the transduction mechanism in *Melanophila acuminata*, we believe that incident infrared radiation produces a strain in the chitin, compressing the dendritic tip, and triggering an action potential. Recently, a MEMS strain gauge has been developed to push the measurement of strain to new limits. Specifically, the strain gauge developed by Wojciechowski et al. is capable of measuring strains down to 33 nano-strain in a 10 kHz bandwidth². The goal of the chitosan coated MEMS strain gauge is to coat this highly sensitive gauge with a thin film of chitosan. The strain gauge itself is a double-ended tuning fork connected to a comb drive which resonates the tuning fork. Strain is measured by the change in the frequency of the resonating tuning fork. By using infrared radiation to strain the chitosan film, and then using the MEMS strain gauge to measure the resulting strain, we can transduce the incident infrared radiation into a frequency modulated signal.

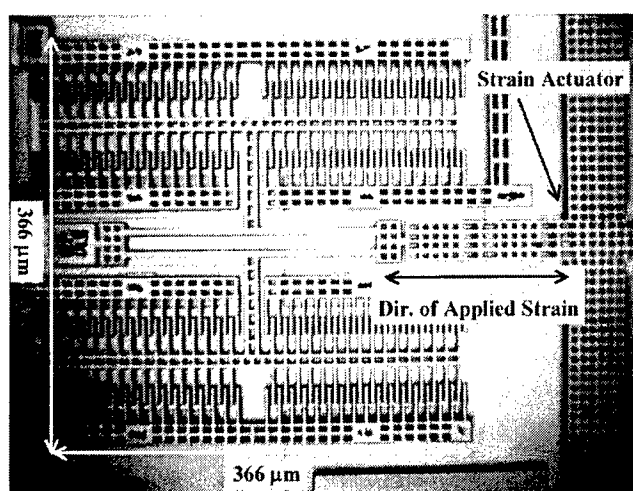


Figure 22: The MEMS double-ended tuning fork resonant strain gauge. Chitosan may be applied over the strain actuator or over the double ended tuning fork itself. Image from Wojciechowski et al.

The strain gauge itself is quite large due to the presence of the comb drive. The gauge has a footprint of 366 μm by 366 μm , as shown in Figure 22. A portion of a strain actuator is shown to the right in Figure 1. This test structure occupies additional die area, and may be coated with chitosan to maximize the amount of applied strain to the gauge. Figure 23 shows a modified version of the strain gauge, where chitosan (shown in red), is placed directly over the double ended tuning fork. As infrared radiation is absorbed by the chitosan, strain is applied in the horizontal direction, which alters the resonant frequency (tuning fork resonates in the vertical direction).

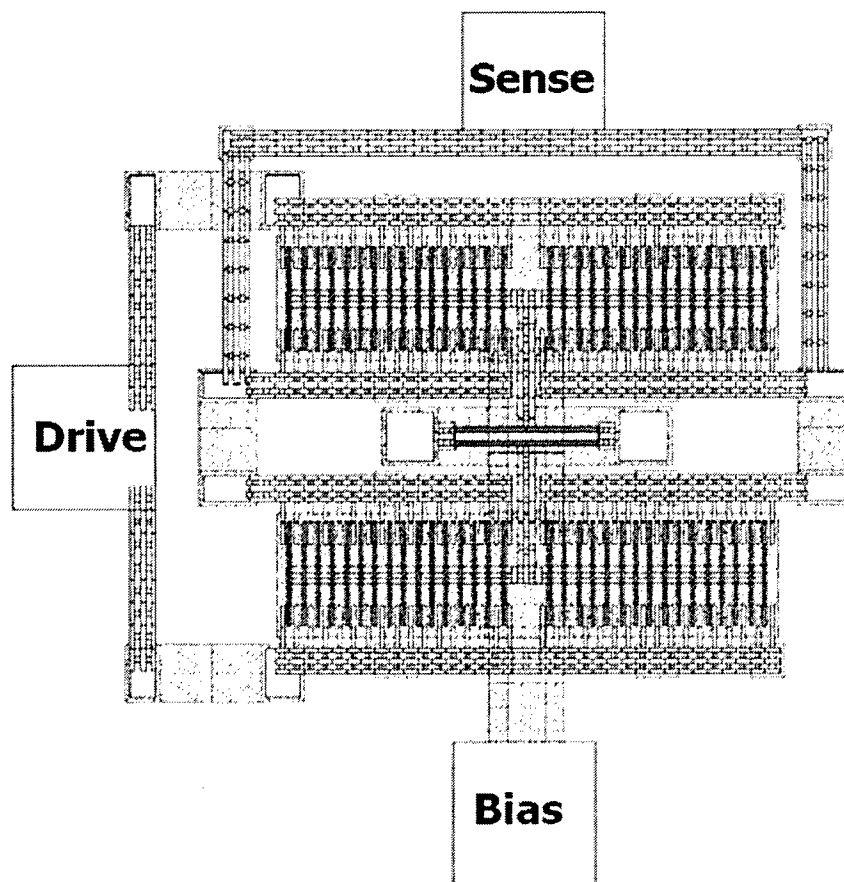


Figure 23: The MEMS strain gauge with chitosan-coated DETF. The device may offer the greatest performance in terms of sensitivity but does so at the expense of size.

Strain Gauge Fabrication Process

The chitosan-coated strain gauge concept uses the highly sensitive strain measurement obtained by resonating a double-ended tuning fork in a MEMS device to indirectly transduce IR radiation by measuring the resultant strain in the chitosan film. The fabrication sequence is shown in Figure 24.

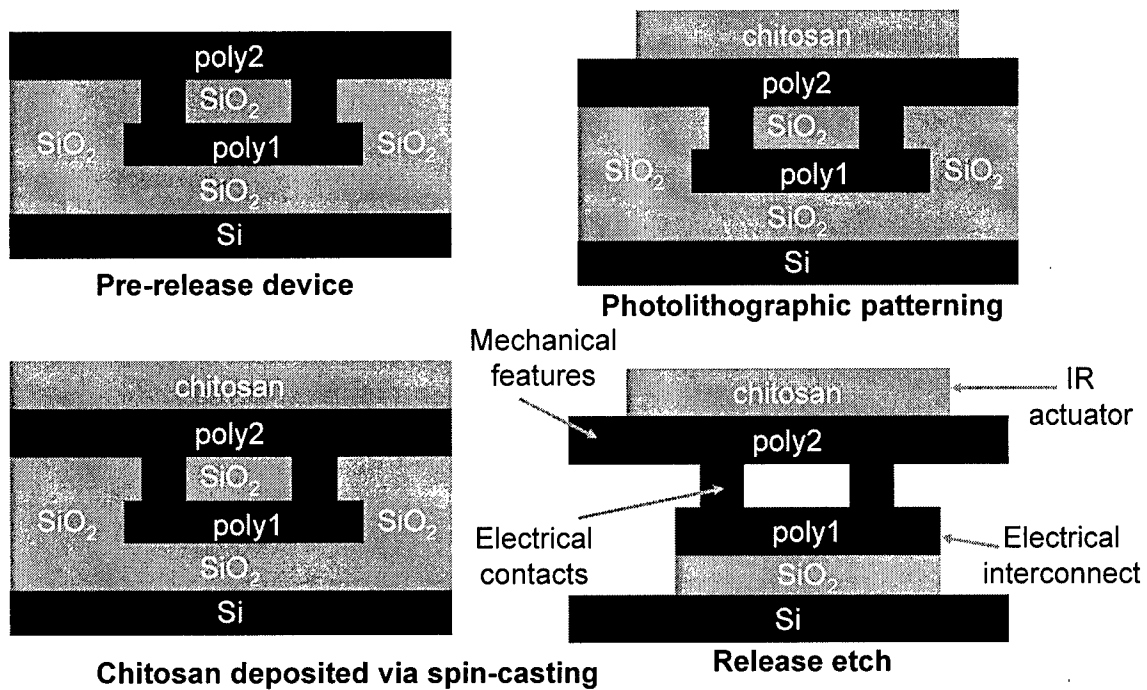


Figure 24: Chitosan-coated strain gauge fabrication process. Chitosan is first photolithographically patterned, then the device is released with an oxide etch.

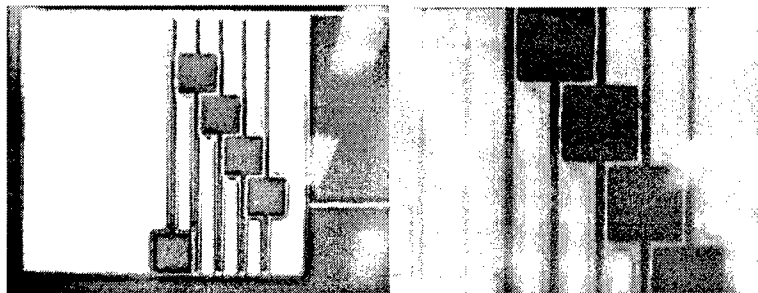


Figure 25: Prefabricated polySi cantilevers (unreleased) with thin film chitosan coating. Proper device formation requires either laser ablation or another lithography step.

The device is fabricated using a commercial foundry process from Bosch, which uses two layers of polysilicon. The unreleased device is then spin-coated with chitosan, and then photolithographically patterned. Following patterning, the sacrificial oxide is etched, releasing the structure.

Device #3: Chitosan Cantilever Infrared Sensor

The concept behind the chitosan-coated cantilever bimorph is to create a thermal detector with high thermal mismatch and hence maximal deflection for a given amount of incident infrared radiation. Thermal sensors generally operate by absorbing infrared or electromagnetic radiation and converting the radiation to heat energy. The heat energy produces a temperature change that is ultimately transduced into an electrical signal. Our goal is to engineer chitosan to maximize the amount of heating for a given amount of incident IR flux, thus providing superior sensitivity like that found in *Melanophila acuminata*.

Polymers in general have a high coefficient of thermal expansion, which when coupled to a material such as polysilicon, which has a very low coefficient of thermal expansion, produces a bending moment that is the thermal bimorph effect. Cantilever structures are relatively simple and therefore allow for ease of customization for length, width, and layer thickness. Readout may be performed optically, hence minimizing the need for complex interfacing circuitry.

To further enhance the deflection, a thin layer of Au may be used as an infrared reflector. The thin layer of Au should be small enough to be negligible in the mechanical sense, while still reflecting infrared photons and hence maximizing the absorption of energy in the chitosan layer.

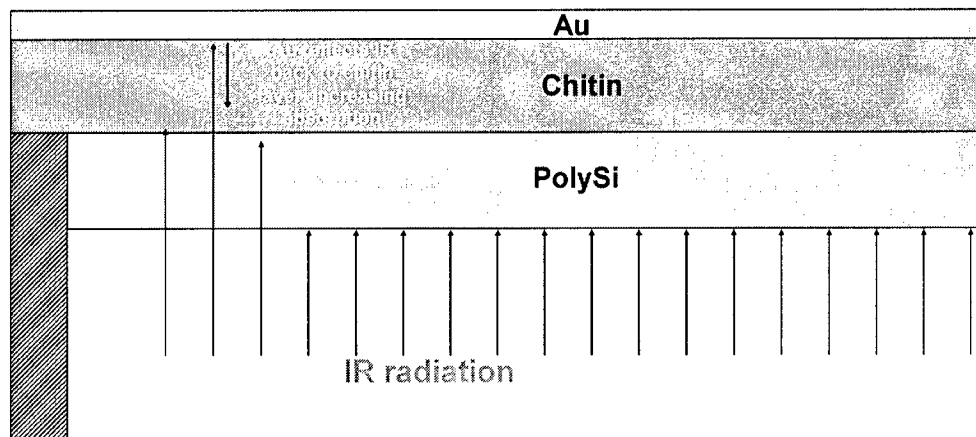


Figure 26: Chitosan-coated bimorph with top Au reflector. IR is applied through the backside (Si and polySi transmit IR).

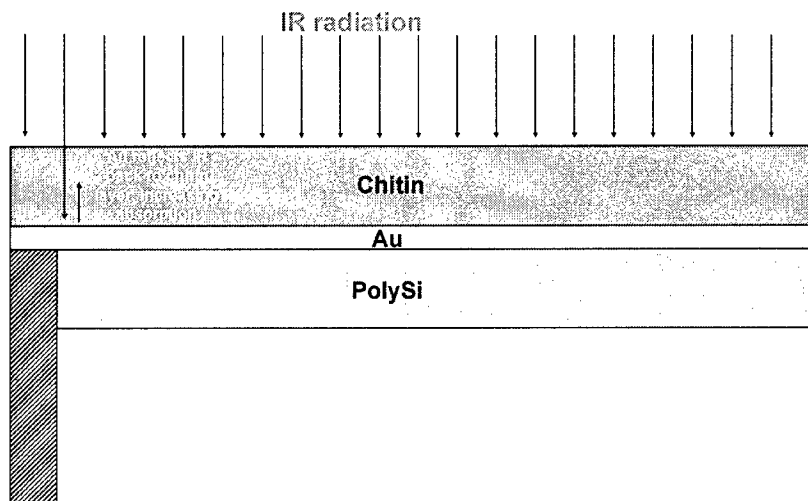


Figure 27: Chitosan-coated bimorph with middle Au reflector. IR is applied through the top and directly absorbed by chitosan. Those infrared photons that are not absorbed on the first pass are reflected and potentially absorbed during the second pass.

We have performed simulations based upon analytical models as well as finite element models for a variety of cantilever material compositions and dimensions. Previous work has examined the possibility of using polystyrene in combination with a variety of semiconductor materials in order to maximize the bimorph effect¹⁰. However, this work using prefabricated AFM tips and is not compatible with photolithography techniques. Simulations were performed for a 100 μm long, 10 μm wide cantilever beam of various thicknesses with an applied radiant

flux of 50 W/m^2 . The Au layers were ignored due to their small thickness relative to the polymer and semiconductor layers.

Cantilever Bimorph Composition	Polymer Thickness	Non-Polymer Thickness	Max Deflection
Polystyrene / PolySi	1 μm	100 nm	13.75 μm down
Chitin / PolySi	1 μm	100 nm	8.54 μm down
Chitin / Au	1 μm	100 nm	7.4 μm down
Polystyrene / Au	1 μm	100 nm	2.081 μm down
Polystyrene / PolySi	100 nm	1 μm	131.6 nm down
Chitin / PolySi	100 nm	1 μm	1.67 nm down
Chitin / Au	100 nm	1 μm	1.393 nm down
Polystyrene / Au	100 nm	1 μm	142.4 nm down

Figure 28: Summary of finite element deflection results for a 100 μm long cantilever beam. Polymer / PolySi bimorph offers substantial deflection for thick polymers. While previous work has looked at using polystyrene, it is not currently compatible with photolithography processes.

Deflection at these power levels is quite significant, and much smaller deflections may easily be detected. Thus, the chitosan cantilever infrared sensor offers promising sensitivity in a compact, batch fabricated device that may use an optical readout rather than complex electronic circuitry.

Chitosan Cantilever Bimorph Fabrication Process

The fabrication of the chitosan cantilever bimorph utilizes standard photolithographic processes. Initially, prefabricated, unreleased polysilicon cantilevers were obtained. Chitosan may be spin-coated over the dies, but patterning the chitosan requires either laser ablation or a matching photomask and another photolithography step (Figure 25).

Therefore, it was decided to fabricate the entire cantilever structure from a custom photomask, using the basic process shown in Figure 29, rather than attempt to add chitosan to an existing cantilever die. This also allows the creation and testing of a variety of devices of various lengths and widths. The advantage of the process shown in Figure 29 is the use of a single lithography step. The photoresist defines the area of the cantilever beams. The chitosan is

then etched, but rather than stripping the photoresist and beginning another lithography step, the same photoresist mask is used and the polysilicon is etched. Subsequently, the photoresist is removed and the device is released using an isotropic HF vapor etch. No mask is necessary because the isotropic etch undercuts, leaving anchors to the substrate. Features are drawn larger

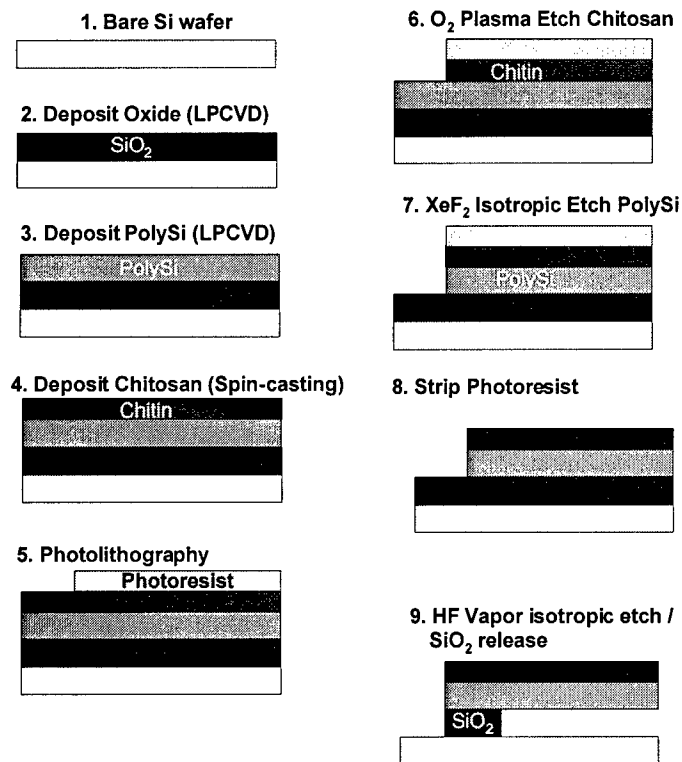


Figure 29: Chitosan cantilever fabrication

to compensate for this undercutting. For simplicity, the PMMA barrier layer as discussed in Figure 6 is not shown.

A thin Au reflecting layer may be added to maximize absorption in the chitosan films. Two variations exist for incorporating a thin Au IR reflector – one process puts the Au on top and one process puts the Au beneath the chitosan. The simplest method for adding the thin Au layer is to sputter or evaporate Au over the chitosan surface following device release. Infrared light is then detected through the backside, being transmitted through the Si wafer and

polysilicon thin film, and being absorbed by the chitosan. Figure 30 shows one additional step which, when combined with the process in Figure 29, adds the Au IR reflector.

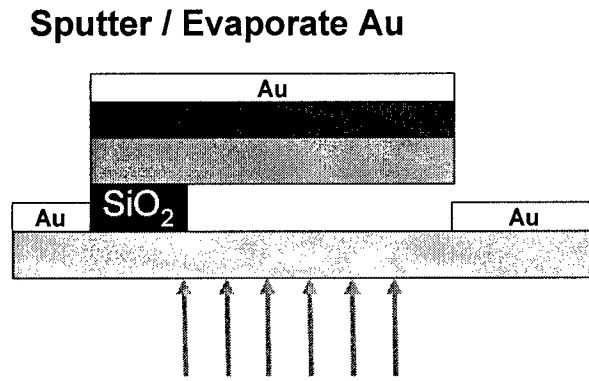


Figure 30: Modification of chitosan cantilever bimorph process to add top Au layer for IR reflection. IR is applied through the backside (Si transparent), and absorbed in chitosan layer.

To allow direct infrared absorption by chitosan without first having to pass through the single crystal silicon and polysilicon, Au may be deposited on top of the polysilicon film and patterned using an aqua regia etch. Following Au patterning, chitosan is deposited by spin-casting and the photolithography and etching processes proceed. Figure 31 shows the fabrication sequence for putting Au beneath the chitosan in the cantilever device. Although the fabrication is slightly more complex, the advantage is that IR light does not need to pass through the backside, potentially making the device more sensitive.

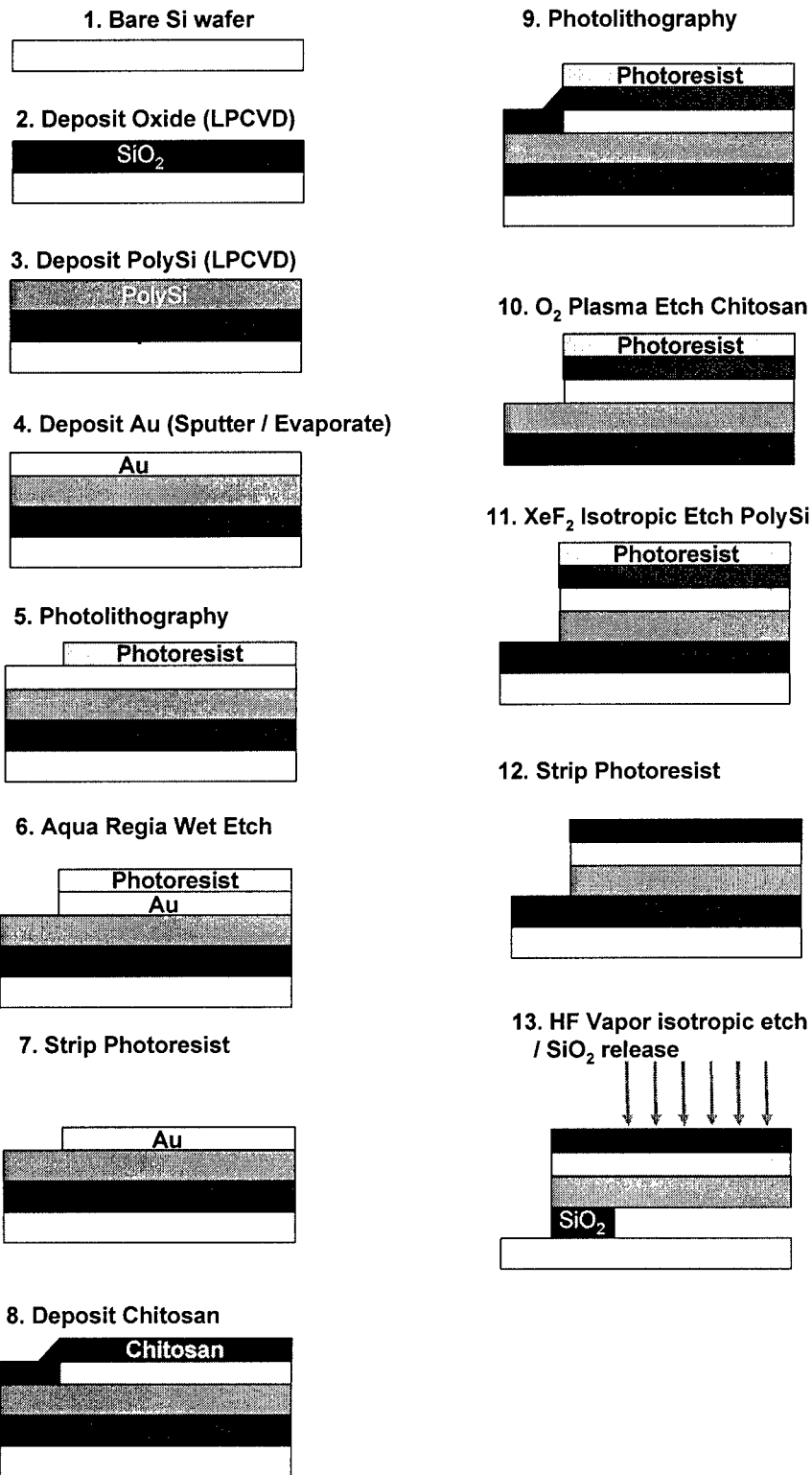


Figure 31: Fabrication process for chitosan cantilever with Au reflecting layer underneath. An additional photolithography step is required by IR may be directly absorbed by the chitosan layer and reflected by the Au layer.

Device #4: Membrane Strain Sensor (Alternate concept)

The chitosan membrane sensor consists of an edge supported chitosan membrane with piezoresistive polysilicon nanowires patterned on the membrane surface. As the membrane strains, a change in resistance is induced in the nanowire. The change in resistance of the nanowire, when measured in a temperature compensated Wheatstone bridge, can compensate for temperature changes in the substrate and will measure incident heat flux / infrared radiation. Aluminum contact pads are used to provide connectivity to the polysilicon nanowires. Figure 32 shows a top and side view of the device on the left, and the device fabrication sequence on the right.

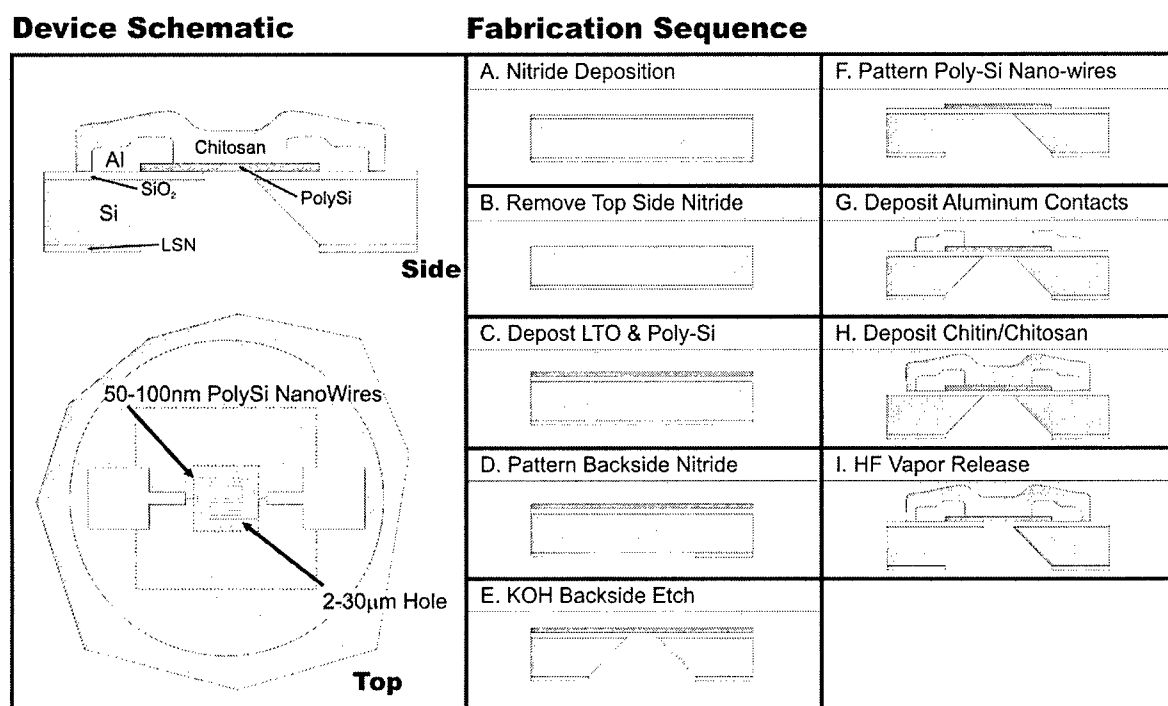


Figure 32: Chitosan Membrane Strain Sensor.

The fabrication sequence begins with growing Low Stress Nitride (LSN) on the backside of the wafer. Next, a 1-2 μm Low Temperature Oxide (LTO) layer is grown on the top surface, followed by a 50-100 nm polysilicon layer. The backside LSN is patterned and a backside through etch using KOH is performed. Now, the polySi is patterned using E-Beam lithography and the aluminum contact pads are deposited. Chitosan will be deposited using spin-casting or by applying a drop directly to the surface using standard laboratory fluidic methods. Finally, HF vapor is used to release the chitosan membranes. Nanowire fabrication using 50-100 nm poly-Si has been demonstrated by I. Park and may be used for the chitosan membrane strain sensor.

References

1. Evans, W.G. Perception of infrared radiation from forest fires by *Melanophila acuminata* de Geer (Buprestidae, Coleoptera). *Ecology*, 47, 1061-1065 (1966).
2. K.E. Wojciechowski, Boser, B.E., Pisano, A.P., "A MEMS resonant strain sensor with 33 nano-strain resolution in a 10 kHz bandwidth," *IEEE Sensors 2005*, 2005.
3. Lorenz, H., Despont, M., Fahrni, N., LaBianca, N., Renaud, P., Vettiger, P. SU-8: a low-cost negative resist for MEMS. *J. Micromechan. Microeng.* 7, 121-124 (1997).
4. Domard, A. & Domard, M. Chitosan: structure-properties relationship and biomedical applications (ed. Dumitriu, S.) (Marcel Dekker, New York, 2002).
5. Wu, L., Yi, H., Li, S., Rubloff, G.W., Bentley, W.E., Ghodssi, R., Payne, G.F. Spatially selective deposition of a reactive polysaccharide layer onto a patterned template. *Langmuir* 19, 519-524 (2003).
6. Fernandes, R., Wu, L., Chen, T., Yi, H., Rubloff, G.W., Ghodssi, R., Bentley, W.E., Payne, G.F. Electrochemically induced deposition of a polysaccharide hydrogel onto a patterned surface. *Langmuir*, 19, 4058-4062, 2003.
7. Fernandes, R., Yi, H., Wu, L., Rubloff, G.W., Ghodssi, R., Bentley, W.E., Payne, G.F. Thermo-biolithography: A technique for patterning nucleic acids and proteins. *Langmuir*, 20, 906-913, 2004.
8. Madou, M. "Fundamentals of Microfabrication," CRC Press, 2002.
9. East, G. C., Qin, Y. Wet Spinning of Chitosan and the Acetylation of Chitosan Fibers. *Journal of Applied Polymer Science* 50, 1773-1779 (1993).
10. M.C. LeMieux, M.E. McConney, Y. Lin, S. Singamaneni, H. Jiang, T.J. Bunning, and V.V. Tsukruk, "Polymeric nanolayers as actuators for ultrasensitive thermal birmorphs," *Nano Letters*, vol. 6, pp. 730-734, 2006.

Personnel Supported:

PI: Dr. Albert P. Pisano

Graduate Students:

Jim Cheng
Michael Mueller
Ya-Mei Chen
Thomas H. Cauley III

Co-PI: Dr. Luke Lee (April 2006)

Staff Scientist:

Dr. Jeonggi Seo (April 2006)

Publications: None

Interactions & Transitions

6/30/2005 Two technical disclosures, entitled 1) Organic IR-Detecting Strain Gauge and 2) Photomechanical IR-Detecting Sensor were filed with the University of California, Berkeley Office of Technology Licensing.

7/7/2005 Provisional patent application entitled Infrared Sensor System and Devices (60/697,741) was filed with the USPTO.

7/8/2005 Professor Albert Pisano presented research thrusts and an overview of the BIRN project at the DARPA BioSenSE Kickoff Meeting in Woods Hole, MA.

8/4/2005 Held technical discussions (video conference) with Kodak scientists based in Rochester, NY. Introduced Kodak team to the BIRN project and discussed current efforts and project milestones.

8/5/2005 Submitted performance report detailing status of effort, accomplishments and new findings, and invention disclosures to AFOSR.

9/19/2005 to 9/21/2005 Presented posters entitled MEMS Biomimetic Infrared Nanosystems (BIRN) and to 20+ BSAC industrial member companies at the Fall IAB Meeting

9/29/2005 Held technical discussions regarding polymers with Kodak scientists based in Rochester, NY.

10/27/2005 Held technical discussions (video conference) with Professor Helmut Schmitz and students at the University of Bonn, Germany. Presented current UC Berkeley work and discussed possible transduction mechanisms and biomimetic approaches.

10/31/2005 Held technical discussions regarding polymers with Kodak scientists based in Rochester, NY.

11/3/2005 Delivered powerpoint presentation to Dr. Morley Stone in response to request for slides for DIRO Review.

12/5/2005 University of Bonn Video Conference

12/5/2005 Presented current research to Dr. Russ Potts and Dr. Mikhail Kouchnir of Vivomedical. Brainstormed potential areas of application for Vivomedical's sensor platform.

1/17/2006 Held technical discussions regarding polymers with Kodak scientists based in Rochester, NY.

1/17/2006 Professor Helmut Schmitz from University of Bonn, Germany, traveled to UC Berkeley to meet with BIRN researchers. Current work by Professor Schmitz and UC Berkeley researchers was presented and future directions discussed.

1/26/2006 Presented current research to Yoshio Okayama of Sanyo. At Mr. Okayama's request, we provided additional information in the form of a powerpoint presentation to be presented by Mr. Okayama to Sanyo Japan.

2/6/2006 to 2/8/2006 Presented posters entitled "Polymeric Strain Infrared Sensor" and "Photomechanical Thin-Film Transistor Infrared Sensor" to 20+ BSAC industrial member companies at the Spring IAB Meeting.

2/9/2006 Provided program manager Dr. Morley Stone an update on research progress in response to the DARPA Winter Review / Congressional briefing.

2/9/2006 An overall BIRN project presentation was presented to Dr. Don Leo, DARPA DSO, because the work was originally funded by the DARPA DSO office.

2/28/2006 At the request of AFOSR, a powerpoint detailing objectives, technical approaches, results-to-date, anticipate results, and Air Force relevancy was submitted to Dr. Hugh DeLong.

3/17/2006 A talk entitled "Polymeric strain infrared sensor inspired by the fire-loving beetle *Melanophila acuminata*" was given at the weekly Nanoscale Research Seminar, University of California, Berkeley by graduate student Michael Mueller.

3/23/2006 Held technical discussions regarding polymers with Kodak scientists based in Rochester, NY.

4/26/06 Professor Albert Pisano and graduate student Jim Cheng presented current research results and an update on the Phase I milestones at the BioSenSE PI Meeting in Arlington, VA. Dr. Douglas Robello of Kodak (Rochester, NY) also presented.

5/5/2006 Held technical discussions regarding polymers with Kodak scientists based in Rochester, NY.

5/5/2006 University of Bonn subcontractors Dr. Michael Tewes and Dr. Markus Lohndorf of cesar traveled to UC Berkeley. An update on current progress and ongoing work at cesar and UC Berkeley was presented.

5/16/2006 Provided a powerpoint presentation to Dr. Carl Kirkconnell of Raytheon to introduce Raytheon to the project and determine possibility of Raytheon assistance in characterizing device response.

6/7/2006 Nonprovisional patent application entitled Infrared Sensor Systems and Devices (60/697,741) was filed with the USPTO.

7/20/2006 Delivered oral presentation to Toyota describing current status of research as well as offering possibilities of future remote sensing capabilities for use in Toyota products.

7/26/2006 Provided powerpoint presentation and proposal to Dr. Howard Choe of Raytheon for possibility Raytheon collaboration on BIRN project.

8/25/2006 Delivered powerpoint presentation to new program manager, Dr. Don Leo, in response to request for project update following April PI Meeting.

9/1/2006 AFOSR / DARPA Annual Report

9/18/2006 to 9/20/2006 Fall IAB Meeting

12/31/2006 AFOSR / DARPA Final Report

Other Events:

8/26/2005 Graduate student Jim Cheng successfully completed his preliminary exams.

3/20/2006 Graduate student Michael Mueller successfully completed his qualifying exam and advanced to Ph.D candidacy.

8/20/06 Graduate student Jim Cheng submitted his Master's Thesis entitled "Chitosan as a MEMS Engineering Material."

New Discoveries, Inventions, or Patent Disclosures:

7/7/06 UCB
U.S. Non-Provisional Patent Application 11/483,142

7/7/06 PCT International Patent Application PCT/US06/26664

Honors/Awards: Albert P. Pisano, Member, National Academy of Engineering
Fellow, American Society of Mechanical Engineers

University of Bonn - Final Performance Report

Introductory Remark:

The project focused on the infrared (IR) sensory systems of so-called pyrophilous insects which show the behaviour to approach forest fires. For this reason, the animals are equipped with IR sensory organs. Compared with uncooled technical IR sensors, the insect IR receptors have some interesting advantages: (i) there is no need for temperature constancy; (ii) the receptors can be operated at high ambient temperatures; (iii) the receptors are rugged having a smart design, and work even under harsh environmental conditions. Additionally, the neuronal network which processes the IR information in the central nervous system of the beetles, obviously can extract the relevant signals from considerable thermal noise.

The objective of the proposed research was to broaden the understanding of the biological significance, special function, and performance of biological IR reception. The final aim of the research was to further develop concepts of uncooled IR sensors which are based on the principles and mechanisms of biological models which were improved by millions of years of evolution. In the focus of interest are so-called photomechanic IR receptors which most probably have evolved from peripheral mechanoreceptors transducing the incoming IR radiation into a micromechanical event which is measured by a sensitive mechanoreceptive sensory cell. To achieve the objectives, morphological as well as neurophysiological investigations have been performed. During the 12-month period of performance, work has focused on the analysis of the photomechanic IR receptors of buprestid beetles of the genus *Melanophila*. Additionally, a variety of other pyrophilous insects from different orders were observed and collected on freshly burnt areas in Western Australia. Some of them were screened for hitherto unknown receptors which may function as IR receptors.

People involved in this research:

Dr. Helmut Schmitz, Co-PI (Bonn University)

Dr. Michael Gebhardt, Senior Scientist (Bonn University)

Dr. Michael Tewes, Team leader at caesar

Dr. Markus Löhndorf, Team leader at caesar

Jörg Scheurer, student (caesar)

Structure and function of the IR sensilla in *Melanophila* beetles

Introduction – Buprestid beetles of the genus *Melanophila* inhabit the palaeartic as well as the nearctic parts of the world. As a special behavioural feature, beetles of both sexes approach forest fires because their brood depend on burnt wood as larval food. Initially, the freshly burnt area serves as a meeting place where the males vigorously search for females. After mating, the females deposit the eggs under the bark of the burnt trees. However, the outbreak of a forest fire is highly unpredictable. In the northern boreal forests, where most *Melanophila* species can be found, a fire statistically occurs only every 50 - 200 years. Because finding a fire is crucial for the survival of all *Melanophila* species, *Melanophila* beetles should be able to detect fires from distances as large as possible. Therefore, it is reasonable to suppose that the sensory organs which are used for fire detection have been subjected to a strong evolutionary pressure especially with regard to sensitivity. For the detection of fires, *Melanophila* beetles are equipped with special antennal smoke detectors⁴ and thoracic IR receptors⁵.

The IR receptors are situated in two pit organs which are located on the metathorax. Each IR organ houses about 70 IR sensilla which are closely packed together at the bottom of the pit⁶. From the outside, a single sensillum can be recognized by a hemispherical elevation with a diameter of about 12 – 15 μm . This dome-shaped elevation is build by a thin epi-/mesocuticle which forms the outer half of the boundary of an internal spherical cavity. The cavity is almost completely filled out by a tiny cuticular sphere with a diameter of about 10 μm . Based on transmission electron microscopical observations,⁷ described that the sphere consists of three different zones: (i) an outer lamellated mantle, (ii) an intermediate layer of unstructured cuticle containing irregularly arranged microcavities, and (iii) a innermost zone where the cuticle appears uniform except for some spots of higher electron density. The sphere is connected to the vertex of the outer cuticular dome by a small cuticular stalk; the narrow gap surrounding the sphere is filled out by leaflike extensions of at least two enveloping cells⁷. In contrast to these findings, it was reported recently that a large air-filled cavity is situated in the centre of the sphere⁸. From below, the sphere is innervated by a single sensory cell. All morphological as well as all physiological data available so far show that this cell most probably is a ciliary mechanoreceptor^{7,9,10}.

Based on the different morphological results, two models of sensillum function exist. However, the models are inconsistent with each other. (i) Vondran et al (1995) proposed the so called photomechanic model (see also Schmitz and Bleckmann 1998) where the biomolecules (i.e. proteins and chitin) of the cuticular sphere strongly absorb mid-IR radiation. In a way not further specified, the resulting thermal expansion of the sphere is measured by the mechanoreceptor. (ii) Assuming the presence of an air-filled cavity inside the sphere, Evans (2005) proposed that IR radiation enters this cavity by a small apical waveguide with a diameter of about 1.5 μm . Due to absorption of IR photons at the cuticular walls of the cavity, the enclosed air is heated up and expands. The resulting increase in gas pressure should stimulate the mechanoreceptor.

In this paper we try to conclusively resolve the details of the transduction mechanisms of the *Melanophila* IR sensillum. For this purpose, we tried to understand the phylogenetic origin of the IR sensilla, which most probably have evolved from hair mechanoreceptors (sensilla trichodea) of the lateral body wall. This approach seemed very promising in *Melanophila* species because in the immediate vicinity of the field of IR sensilla at the bottom of the pit organ, so-called intermediate sensilla can be found⁷. The cuticular apparatus of those intermediate sensilla show – at a variable degree – features of hair mechanoreceptors as well as features of IR sensilla. The study of such intermediate systems and of fully developed hair mechanoreceptors should help to comprehend the gradual transition from a well-known hair mechanoreceptor to an IR sensillum. Furthermore, the morphology and ultrastructure of the IR sensilla were investigated with a variety of different methods.

Material and Methods

Animals

Adult beetles hatched from burnt logs which were stored in the animal house of the Zoological Institute. The wood originated from forest fires happening in summer 2002 and 2003 respectively. Animals were kept for several weeks in plastic boxes and fed with raisins, peanuts and walnuts. Water was given ad libitum.

Scanning electron microscopy

Beetles were cleaned by sonication in a mixture of chloroform / ethanol (2:1) for 2 min. After drying, specimens were glued on holders with carbon glue (Leit-C, Fa. Neubauer), sputtered with gold, and examined in a LEO 440i (Leica, Bensheim, Germany) scanning electron microscope (SEM).

Focused ion beam (FIB) technique

The cross-sections were prepared with the focused ion beam (FIB) machine LEO 1540XB by Zeiss. This device allows the ablation of probe material by a focused ion beam with a resolution better than 50 nm. Simultaneously the probe can be imaged by a scanning electron microscope (SEM) to control the milling process. The electron beam of the SEM is tilted by 54° with respect to the ion beam.

All preparations with the FIB were done in the “milling for depth” mode with the milling depth parameter set to 25 nm in Silicon. Prior to the cross sections a coarse milling step was performed in front of the region of interest to remove material that would otherwise block the sight of the SEM. For that purpose the beam parameters were set to 10 nA and 30 kV. The coarse milling was stopped 2 μm in front of the region of interest and the current was reduced to 1 nA for the following fine milling. The milling was interrupted every few nanometers to take an intense secondary electron picture by the SEM with 5 kV acceleration voltage, an aperture of 120 μm and activated high current option.

Light and transmission electron microscopy

Sensory IR pit organs from 6 beetles together with about 0.5 mm of surrounding cuticle were excised in iced glutaraldehyde fixative (3% glutaraldehyde in 0.05 mol l⁻¹ cacodylate buffer, pH

7.1; osmolarity 380-400 mosmol l⁻¹) and fixed overnight. The organs were then washed in buffer, postfixed with 1.5% OsO₄ in the same buffer, dehydrated through an ascending ethanol series and embedded in Epon 812. Semithin and ultrathin sections were cut with a Reichert Ultracut Microtome using glass- or diamond knives. Semithin sections (0.5 µm) were stained with a 0.05% toluidine-blue/borax solution and examined with a Leitz DM RBE light microscope. To show the different types of cuticle, the Epon resin was removed in some sections by immersion in an alcoholic KOH solution. After washing in 96% ethanol, sections were stained with a Mallory trichrome solution for 5 min. Digital images of the sections were taken with a Nikon Coolpix 5000. Ultrathin sections were stained with uranyl acetate and lead citrate and examined with a Zeiss EM 109 TEM.

Sections were taken from 10 IR organs. Longitudinal as well as transverse sections were cut through IR sensilla, intermediate sensilla and hair mechanoreceptors.

Results and Conclusions

The paired IR pit organs (about 0.1 mm deep) are located at the anterior rim of the metathorax adjoining the coxae of the middle legs (Fig. 1a). Towards the mesothoracic coxal capsule, the pits are demarcated by a steep edge. From the height of the adjoining metathorax, the surface slopes down somewhat more gradually towards the bottom of the pit. Fully-developed IR sensilla associated with wax glands are located at the bottom of each pit organ. From outside, a single IR sensillum is characterized by a dome-shaped elevation with a small apical depression. Each sensillum is accompanied by a wax gland (Figs. 1a, b). Furthermore, the state of development of IR sensilla within a given organ is not uniform. Looking at the size and the symmetry of a sensillum we found that sensilla in the dorsal region are larger and show a better state of development than sensilla located in the ventral half. This can be noticed also in the organ shown in Fig. 1 a. During our examinations of IR organs in different beetles it was striking that we also found a number of malformed organs (Fig. 1 e).

The top edge of the posterior slope bears some hair mechanoreceptors (sensilla trichodea) which are also associated with wax glands (Figs. 1a, d). Such contact mechanoreceptors are distributed all over the body of *Melanophila* beetles. Additionally, sensilla can be found which represent

incompletely developed (in the following called “underdeveloped”) IR sensilla. We classified those sensilla into (i) “intermediate” sensilla which show features of hair mechanoreceptors as well as features of IR sensilla and (ii) “hidden” sensilla where the spheres are sunken into the surrounding cuticle to a variable degree. Mostly, the intermediate sensilla can be found at the ventral edge of the IR sensilla field. In some beetles, a small group of more or less well developed IR sensilla can be identified showing a bristle of different length. The bristle arises from the small apical depression on top of the dome (Fig. 1b). Hidden sensilla can mainly be found on the ventral half of the posterior slope (Figs. 1a, c). They represent underdeveloped IR sensilla, which are partially (see Fig. 1 c) or completely (see Fig. 1 d) sunken into the cuticle (see also Fig. 4). The extent of sinking is correlated with the distance of the sensillum to the bottom of the pit (cf. Fig. 1a).

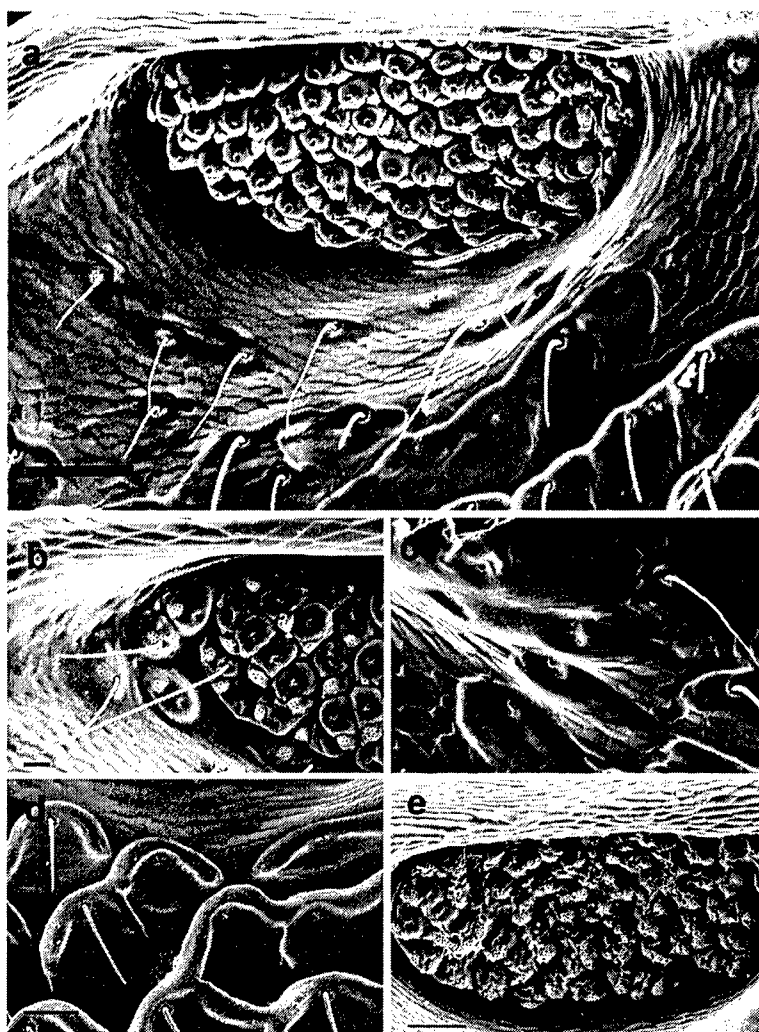


Fig. 1: (a) Outer morphology of the IR pit organ of *Melanophila acuminata*. Dorsal is on the left, ventral on the right. (b) Intermediate sensilla at the ventral edge of an IR organ. (c) more or less hidden sensilla located on the posterior slope of the organ. (d) totally hidden sensilla at the posterior top edge of the pit organ. (e) malformed IR organ. Wax glands are extremely hypertrophied.

By a combination of light- and electronmicroscopical techniques as well as FIB investigations in a SEM, the inner composition of an IR sensillum was unravelled. It could be shown that the outer lamellated mantle of the internal sphere consists of hard exocuticle (Figs. 2a, b) which is heavily reinforced by stacked layers of chitin fibres. The layers change their orientation in a highly regular manner. This is the reason for the lamellated appearance of the mantle when the sphere is sectioned (Fig. 6 c). It is postulated that the outer mantle builds a kind of pressure chamber maintaining a constant volume even if the sensillum heats up a bit. Enclosed by the mantle, a mass of much softer mesocuticle is situated (Figs. 2a, b; 6b) which shows many microlacunae and nanocanals (Fig. 3). All data indicate that these internal hollow spaces communicate with each other and are filled with fluid (mainly water). From the apical depression of the sensillum, a small column of yellowish exocuticle extends into the centre of the sphere (Fig. 2b). It is postulated that this portion of exocuticle represents the remnants of the former bristle of the mechanosensor.

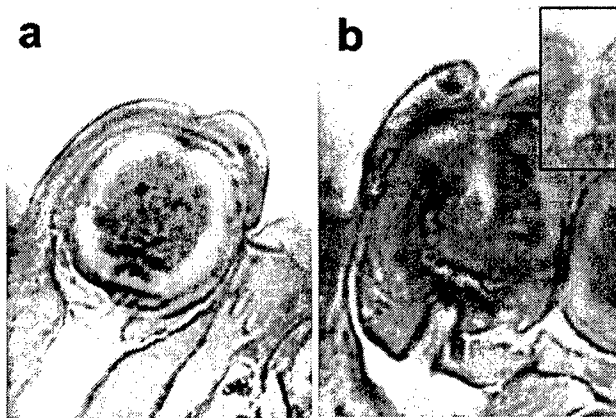


Fig 2: (a) Eccentric semithin section through a single IR sensillum. Mallory stain indicates an outer (yellow) mantle of hard β -sclerotized exocuticle. The inner (red) region most probably consists of softer mesocuticle. (b) Section through the core of an IR sensillum. The innermost small area consists of the remnants of the former bristle of the hair mechanoreceptor (yellow, see also inset). The inner pressure chamber is also well visible.

In the lower part of the sphere, a well-defined cavity can be found which we termed the inner pressure chamber (Figs. 2b, 3).



Fig 3: FIB image of an IR sensillum. The porous structure of the middle mesocuticular region as well as the inner pressure chamber can be seen.

The outermost tip of the mechanosensitive dendrite extends through the outer mantle and finally ends up in the pressure chamber. The dendritic tip contains a tubular body which is a characteristic feature in all cuticular insect mechanoreceptors. The tip is enclosed and supported by fibres which most probably stem from the former joint membrane of a hair mechanoreceptor. The analysis of hair mechanoreceptors, where the dendritic tip is directly attached to the base of the bristle (Fig. 5a, b) revealed that in an IR sensillum the tip of the dendrite has detached from the cuticle and has become enclosed by the former joint membrane of the mechanoreceptor (see Fig. 5b). However, the amount of chitin fibres in this membrane seems to be reduced. Consequently, in an IR sensillum, the mechanical stimulus is transmitted to the dendrite by the joint membrane and/or the surrounding fluid.

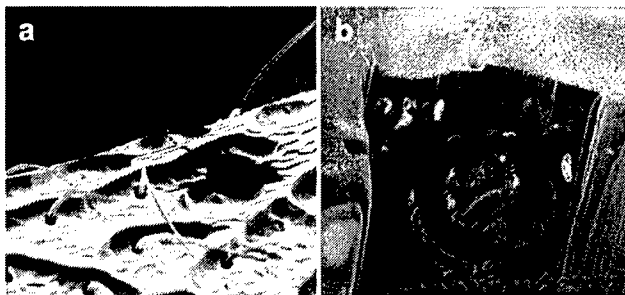


Fig. 4: FIB image of a hidden sensillum located at the posterior upper edge of the IR organ, (a) overview, (b) detail: the sphere inside the cuticle can be seen.

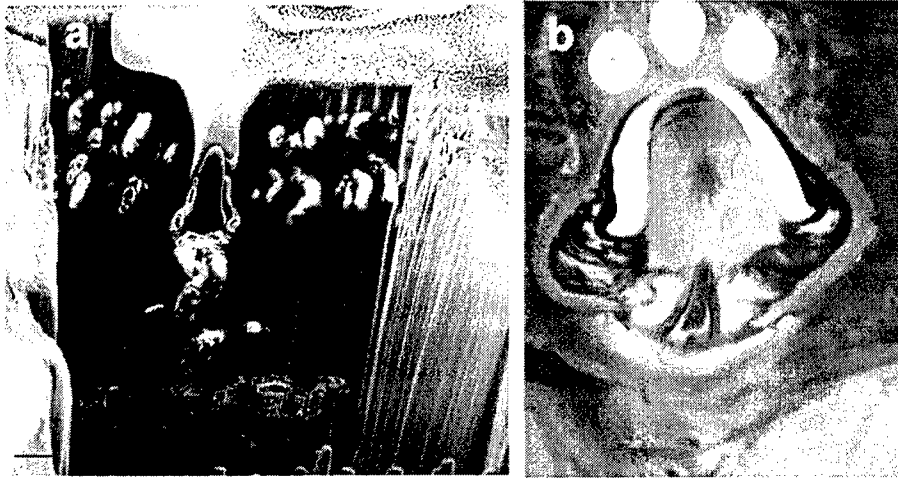


Fig. 5: FIB image showing the base of a hair mechanoreceptor located about 12 μm under the surface of the cuticle; (a) corresponding TEM image also showing the outermost tip of the mechano-sensory dendrite anchored inside the cuticular base of the bristle (b). The base of the bristle is suspended by a flexible membrane which contains many (dark) chitin fibres.

The analysis of the underdeveloped sensilla which are hidden under the cuticle at the posterior edge of an IR organ, gave insight into the developmental processes which are necessary to create an IR sensillum. The bases of the hair mechanoreceptors are located about 12 μm under the surface of the cuticle (Fig. 5a). Considering the conditions in the most underdeveloped IR sensilla where the spheres are totally hidden in the cuticle (cf Figs. 4, 6a) it can be deduced that the base of the former hair mechanoreceptor is the starting point of the formation of the sphere whereas the bristle becomes reduced. The formation of the inner pressure chamber and the retraction of the dendritic tip from the cuticle are the next important steps which most probably happen simultaneously.

Centrifugally arranged nanocanals extend through the outer lamellated mantle of the sphere of an IR sensillum (Fig. 6c). It is postulated that these canals represent a kind of inbuilt low pass filter for compensatory movements of minimal amounts of fluid in and out of the sphere. If it should turn out that this assumption is true, the IR sensillum is equipped with a mechanism to compensate for low frequency changes of the ambient temperature which will not result in a

stimulation of the mechanoreceptor because the pressure within the inner pressure chamber remains constant.

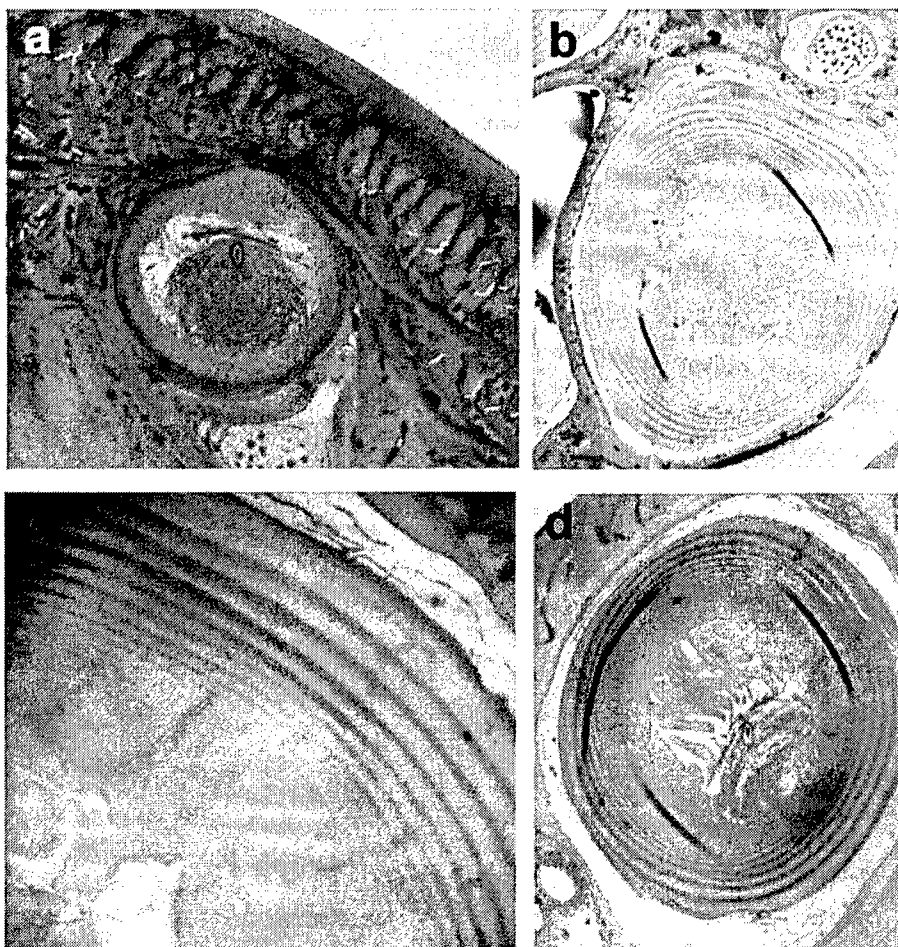


Fig. 6: (a) Section through the inner pressure chamber of a hidden sensillum. The tip of the mechanosensory dendrite is already densely enclosed by fibres of the former joint membrane. (b) Horizontal section through a fully developed sphere of an IR sensillum (c) Detail of the outer lamellated mantle of the sphere showing some centrifugally oriented nanocanals. (d) Horizontal section through the inner pressure chamber of a fully developed IR sensillum. The cross-sectional profile of the dendritic tip enclosed by dark fibres of the former joint membrane is visible inside the inner pressure chamber.

Summary – The thoracic infrared (IR) sensilla of the pyrophilous jewel beetle *Melanophila acuminata* most likely have evolved from hair mechanoreceptors (sensilla trichodea). In a comparative study the morphology the IR sensilla and of neighbouring hair mechanoreceptors

were investigated. It was assumed that any deviation from the *bauplan* of a sensillum trichodeum is of particular significance for the transduction of IR radiation into a mechanical stimulus. Structures supposed to be relevant for stimulus uptake and transduction were homologized. Striking differences like the formation of a three-layered cuticular sphere, the detachment of the tip of the mechanosensory dendrite from the cuticle and the direct connection of the dendritic tip to the remnants of the former joint membrane could be identified in the IR sensilla. Additionally, the dendritic tip has become enclosed inside the sphere in a fluid-filled chamber. As an important functional feature, this chamber communicates with a system of fluid-filled microlacunae and nanocanals extending within the middle layer of the sphere. The biopolymers of the cuticle as well as the water strongly absorb mid IR radiation. Hence we propose that the IR sensilla most probably act as microfluidic converters of infrared radiation into an increase in internal pressure in sphere mediated by a fluid which is measured by the mechanosensitive neuron.

Infrared receptors in pyrophilous bugs

During the field research performed in Western Australia in February 2006 certain species of highly pyrophilous aradid bugs (family Heteroptera) were found on freshly burnt areas. Up to now, pyrophilous behaviour has not been reported for Australian bugs. An in-depth survey for sensilla which may act as IR receptors revealed a hitherto unknown sensillum which is distributed all over the body of the bugs (Fig. 7).

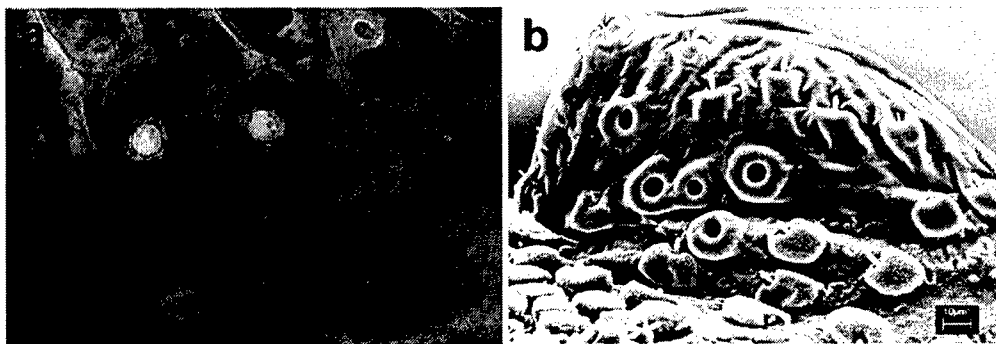


Fig. 7: Lightmicroscopical and SEM-image of the newly discovered sensillum in an Australian aradid bug. A round area of about 5 μm diameter is surrounded by a massive ring of hard cuticle. The central area is hemispherically bent inwards.

A second form of the unknown sensillum was discovered on the lateral body wall of the thorax in the bug (Fig. 8). Interestingly, this form closely resembles the IR sensilla of *Melanophila* beetles (Fig. 9). Because there is already strong evidence that the bug sensillum also has evolved from a hair mechanoreceptor, it is postulated that the unknown sensilla in the bug also act as photomechanic IR receptors. This hypothesis has to be tested by physiological experiments.

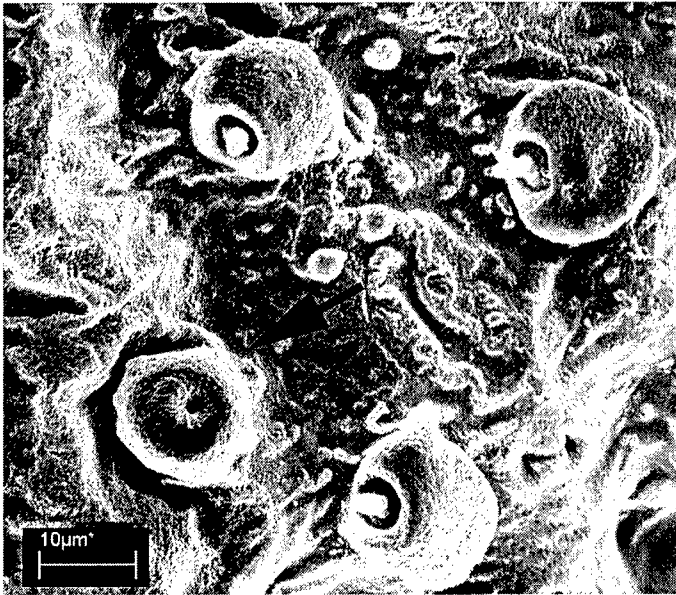


Fig. 8: Amongst small hair mechanoreceptors which are discernible by a tiny bristle, a second form of the unknown sensilla (little spheres with a small apical depression, see arrow) can be found.

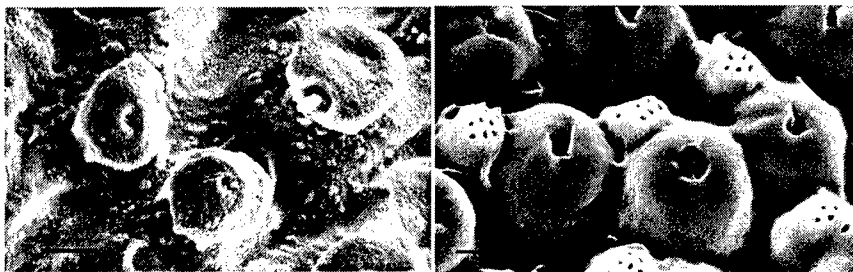


Fig. 9: The spheres found on the lateral body wall of the bug (left image) a reminiscent of the *Melanophila* IR sensilla (right image).

Physiology: Electrophysiological recordings

1. Introduction

The study of the infrared (IR) sense of *Melanophila* encompasses several experimental approaches, one important of them being the electrophysiological analyses of the neural tissue which receives and processes the IR information. There are two levels of interest, (a) the primary sensory neurones which transduce IR radiation into electrically coded neural information. (b) The central nervous networks, which further process the information provided by the primary sensory neurons. The latter is as vital as the former is, since an understanding of the neural processing principles is likely to teach us about novel and effective analyses algorithms. It might even draw our interest to stimulus parameters most relevant to the organism and, thus, to a potential technical innovation, but which have so far been neglected.

2. General methodological remarks

The work reported here has concentrated on the development and the utilisation of intracellular single cell-recording techniques. Previous work on the *Melanophila* IR-organ has yielded a rich set of information on the sensory coding properties of the primary sensory IR-neurons (Schmitz and Bleckmann 1997, Schmitz and Bleckmann 1998, Schmitz *et al.*, 2000). It has exploited the advantages of extracellular single cell-recording techniques including the quick and quasi non-invasive registration of sensory graded potentials and sensory action potentials. There are, however, two drawbacks of the extracellular approach, which make the intracellular approach the first choice: Firstly, it can not be excluded that the sensitivity of the sensory neurons measured with extracellular metal electrodes is lower than the real one, because the electrodes might act as heat conductors, thus, draining off energy from the IR-organ. Secondly, extracellularly measured potentials depend on a multitude of parameters quite difficult to control, like the distance and the electrical conductivity between the source of the potential and the electrode. This prohibits the measurement of absolute potential changes and neuronal noise and, thus, impedes the calculation of figures of merit derived from these absolute measurements, like the standardized detectivity, D^* .

To conclude, the main goal of the ongoing beetle season 2006 is to invent, to implement and to test traditional and novel intracellular recording techniques for the registration of absolute membrane potential changes in IR-processing neurons. The supply with *Melanophila* beetles was, in opposition to our positive experience in former years, insufficient to fully reach this goal in 2005, because only about 20 beetles hatched between July and September 2005. Roughly 100 beetles have hatched so far from our colony of beetle larvae, which provides a substantial basis for considerable experimental headway.

3. a) The primary sensory neurons

As most other neurons do, the primary sensory IR-neurons of *Melanophila* respond to changing IR radiation levels with graded potential changes as well as with frequency modulations of their action potentials fired in response to an IR stimulus. Both parameters can, therefore, be used for an evaluation of the performance of the sensory neurons. There is, however, one caveat to keep in mind: Action potentials as all-or-nothing events are subject to a threshold below which action potentials can not be fired. This can be interpreted as a biological safety measure which ensures that an organism does not overreact in response to a weak, behaviourally irrelevant stimulus. This safety mechanism might obscure the actual maximum sensitivity of the sensory neurons. As a first approach, it is, thus, desirable to measure the graded neural responses to IR stimulation.

This has to be done as close as possible to the site of the mechano-electrical transduction, i.e. close to the sensory dendrite in the cell bodies of the neurons. Our TEM sections through the IR organ reveal that the sensory epithelium which houses the cell bodies, is about 10 to 15 μm in thickness. An intracellular electrode aiming at the cell bodies has to be positioned extremely precisely just above the surface of the tissue followed by an acceleration over a very short distance (approx. $< 5 \mu\text{m}$), but high enough to penetrate the sensory cell bodies. The feasibility of this approach has been tested in the hypodermis of the longhorn beetle *Halotrupes bajulus*, which contains the cell bodies of mechanosensory hair neurons. These experiments clearly ruled this conventional approach out, mainly because the manually accelerated electrode tips

traveled over distances long enough to propel the tips through the hypodermis into the cuticle behind. It has to be added that manual tapping is a widely used and generally accepted technique in insect neuroscience.

Our escape strategy involves two approaches which both rely on a semi-intact preparation of the *Melanophila* IR-organ (see Figure 10). This new preparation is necessary to expose the sensory tissue of the organ, which is *in vivo* occluded by thoracic muscles and tracheal sacs, to the electrode, which, in turn, can not be inserted through the cuticle from the outside. Once an organ is prepared this way, two different techniques will be employed in parallel to record from the sensory cell bodies:

(i) Conventional sharp electrodes as successfully used for recordings from central nervous interneurons (see 3. b), will be positioned on the tissue surface and they will then impale the membrane of a cell body. To avoid the problems discussed above, electrode tips will not be accelerated manually, but will be driven into the cell by means of a 'nanostepper'. Nanosteppers are able to control very fine movements in the nanometer range and they can apply high accelerations over a short distance. We have chosen an 'inchworm' motor (EXFO/Burleigh, Quebec, Canada) as one of the best and reliable devices to accomplish sharp electrode recordings.

(ii) Patch electrode recordings from the neuronal cell bodies will be performed. The major advantage of this approach is that the electrical contact between electrode and the inner of the neuron is not established by a mechanically delicate, high acceleration of the electrode tip, but by suction applied to the electrode. The patch electrode, the position of which is again controlled by an 'inchworm' motor, will be positioned on the surface of the tissue. Once the electrode tip is sufficiently close to the membrane of a sensory cell body, suction seals the contact between electrode and cell membrane which usually splits open under these conditions. The distance between the electrode tip and the cell membrane and the impedance of the seal can easily be monitored by a square voltage pulse applied to the electrode, which will increase in amplitude with decreasing distance. We have already tailored promising patch pipettes which are very likely to yield stable patch recordings.

3. b) Central nervous interneurons

As outlined above, central nervous interneurons form an analysing neural network which extracts the biologically relevant parameters from the IR stimuli. Since it became clear that the *Melanophila* IR sensilla stem from mechanosensory hair neurons (Vondran *et al.* 1995) it is plausible to assume that the topology of these neural networks resembles closely the one of central mechanosensory networks. This is further corroborated by a neuroanatomical study (Gronenberg and Schmitz, 1999): The central nervous projections of the primary IR sensilla are restricted to well-documented, principal mechanosensory neuropils of the thoracic ganglia, but the projection pattern is, nevertheless, clearly distinct from that of other mechanosensory neurons. An extensive search for IR-responsive interneurons may thus become necessary. This study furthermore revealed that the primary IR projection are extraordinarily fine (around 1 μm in diameter). Most of this year's *Melanophila* season is, thus, devoted to further optimise the tips of the electrodes. We succeed so far to produce electrodes with tip diameters smaller than 100 nm. Besides stable recordings from motoneurons, which are comparably large (process of around 3 to 5 μm), we now succeed to record from small-calibre interneurons, whose processes range between 1 μm and 2 μm and which lie, thus, in the size range of the primary IR sensory fibres. We consider this as a major breakthrough in the electrophysiological analysis of the neural IR networks of *Melanophila*.

A detail of a recent recording from an interneuron in meso-/metathoracic is shown in Figure 11 a. This neuron had on ongoing activity of about 20 spikes per second; visual stimuli like moving objects in front of both compound eyes (red bar in Fig. 11 a) elicited short bursts of spikes, which were followed by an inhibition. This recording was stable for about 30 minutes and the resulting staining with the dye Lucifer Yellow shows two intersegmental interneurons with cell bodies in the meso-/metathoracic ganglion and axons ascending to the prothoracic ganglion (Figure 11 b). The fact that more than one interneuron show up in this preparation, is most likely due to dye-coupling between both cells. The neurites of the interneurons at the putative penetration site (marked with ? in Figure 11 b) have diameters of around 1 to 2 μm .

4. Conclusions

The goal of foremost importance of the electrophysiological survey of the *Melanophila* IR-processing system is the calculation of figures of merit like D^* . This enables for the first time to compare the performance of technical IR sensors to that of *Melanophila* IR-sensitive neurons. Four major advances have fostered the feasibility of this goal:

(i) Our collection of scorched logs from wildfires in Catalonia, Spain, is a reliable source of *Melanophila* beetles. We have, thus, experimental animals numerous enough to further tackle the experiments outlined above.

(ii) We have developed electrodes suitable to record from the fine IR sensitive neurons in the *Melanophila* nervous system. It can be expected that we succeed to characterise first IR interneurons during the current beetle season.

(iii) A novel semi-intact preparation of the *Melanophila* IR-organ will enable access to the cell bodies of the sensory neurons. The patch recording from these cell bodies will eventually result in the calculation of technically relevant parameters.

(iv) Both electrophysiological approaches, patch recordings and recordings with sharp electrodes, will be brought forward by the use of a nanostepper.

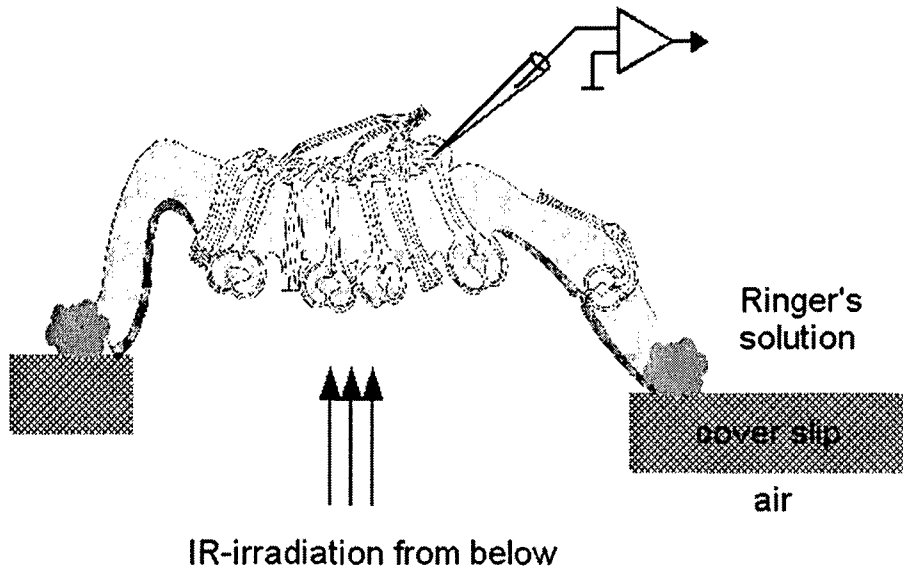


Figure 10: Sketch of the semi-intact, 'inside-out' preparation of the *Melanophila* IR-organ. The organ is either glued to a glass holder made from cover slips as shown in the diagram, or the thoracic cuticle is used as a container for the organ.

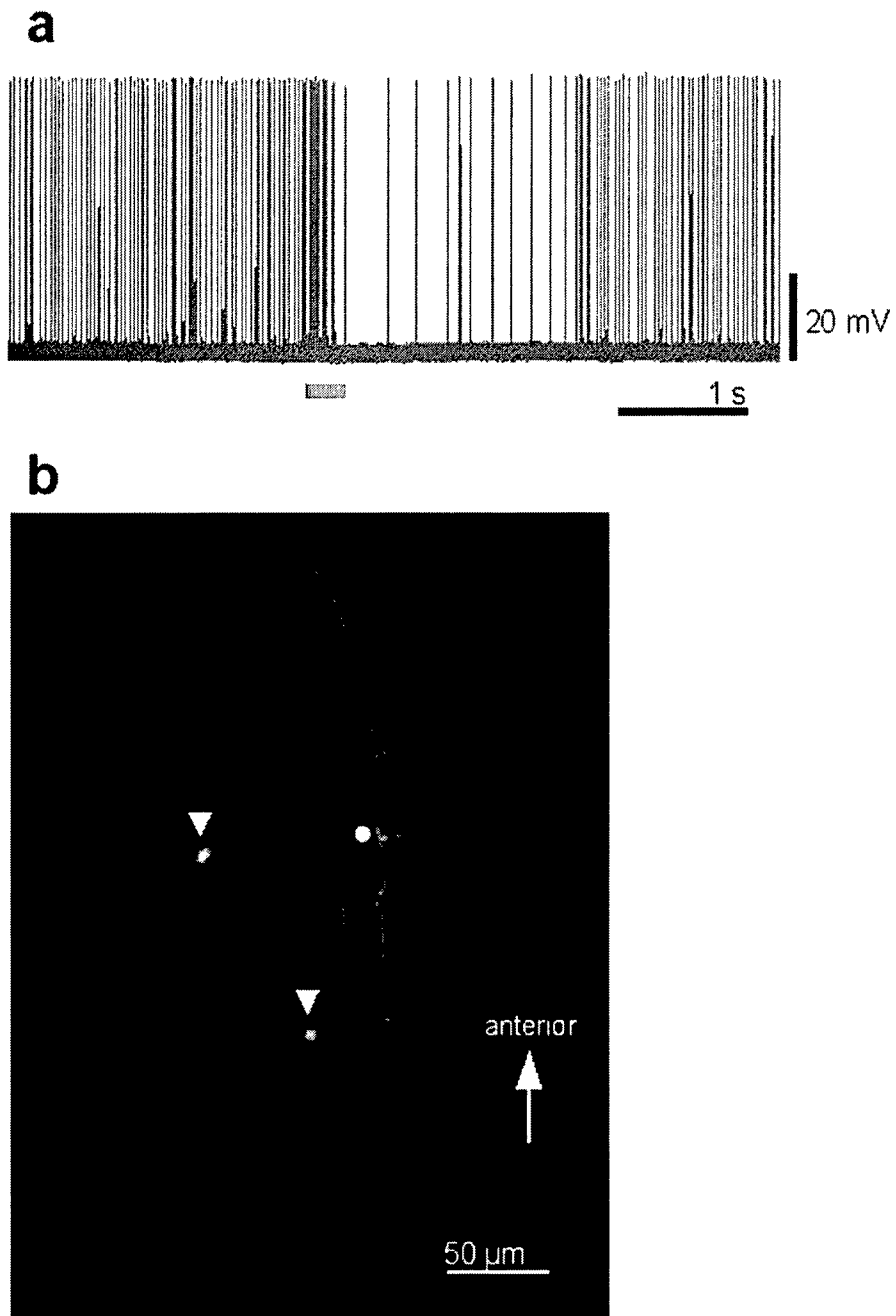


Figure 11: Intracellular recording (a) and staining (b) of a visual intersegmental interneuron in the meso-/metathoracic ganglion of *Melanophila*. a, red bar indicates a period of visual stimulation (moving hand). b) arrowheads, cell bodies of two interneurons, which were presumably dye-coupled. The dot indicates the putative penetration site.

Caesar - Final Report IR-Sensor Project

Period 07/01/2005-06/30/2006

1.) Objectives

The objectives for this reporting period have been:

- to fabrication a miniaturized sensor elements for test purposes,
- to test, if a sufficient signal to noise ration can be obtained by the proposed signal transduction mechanism
- to test the D^* -value of the sensor elements
- support the basic research at the University of Bonn with analytical preparations of *Melanophila* sensila by focused ion beam.

2.) Status of effort

Figure 12 shows the final CAD-design of the sensor element (z-axis is not drawn to scale). The working volume can be seen in the center of the right magnification.

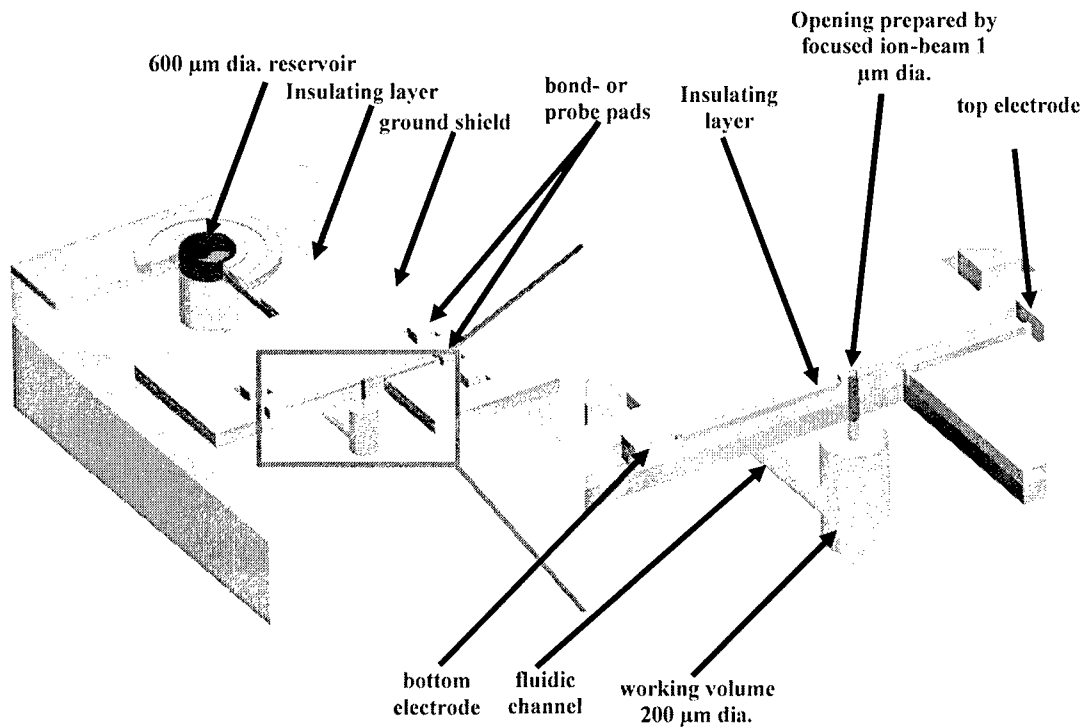


Figure 12: The CAD design of a single sensor element. The right magnification shows the working volume that is confined on the top by the orange SiO₂ membrane and on the bottom by the turquoise Pyrex window. A 1 μm hole is drilled by a focused ion beam into the SiO₂ membrane and both electrode layers on its top.

Using a 500 μm Si-Wafer with a 2.5 μm oxide-layer as substrate, a six step fabrication process has been developed to build the sensors:

- 1.) deposition and lithographic structuring of the first electrode layer (250 nm gold, lift-off),
- 2.) deposition and structuring of an isolating layer (150 nm SiO₂, lift-off),
- 3.) deposition and structuring of the second electrode layer (250 nm gold, lift-off),
- 4.) reactive ion etching from the backside to create the reservoirs and the fluidic channels,
- 5.) focused ion beam etching to create the detection capillary,
- 6.) bonding of Pyrex wafer to the backside to close the fluidic structures.

A set of five lithographic masks was designed to fabricate the sensors. To reduce the number of iteration cycles in the sensor design, twelve design variations have been realized on these masks. Several wafers have been processed successfully in the caesar clean room.

Each wafer consisting of 24 chips with 6 sensor elements each. A single sensor element is shown in Fig. 13.

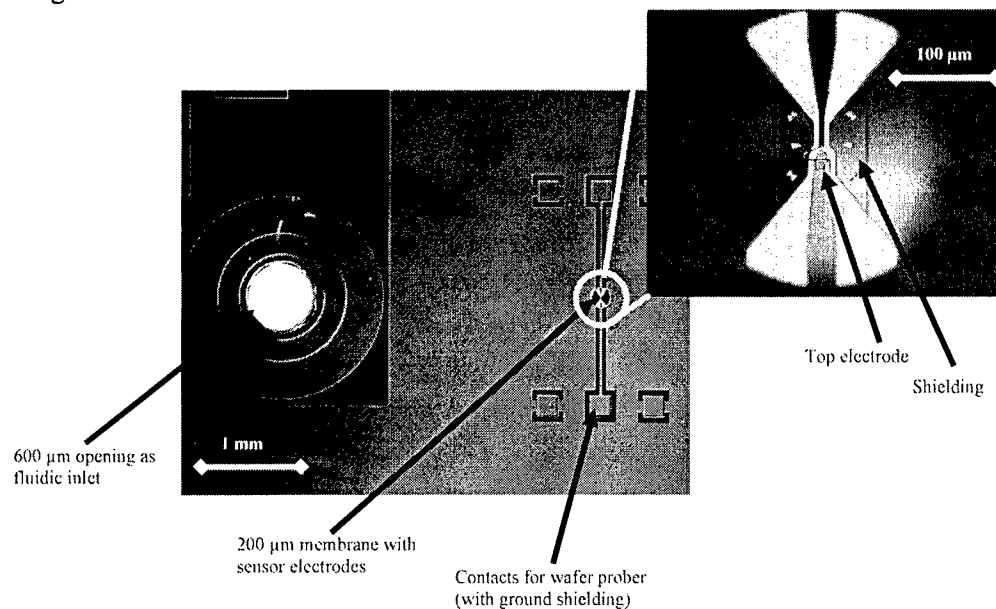


Figure 13: Micrograph of a single sensor element. The right magnification shows the 200 μm diameter working volume that is etched through the wafer. The regions of the working volume that are not covered by a metallization on the top SiO₂ membrane are light up by the back side illumination.

The detection capillaries were prepared by a focused ion beam. Preliminary test have shown that it is possible to drill holes as small as 200nm diameter into the 2 μ m thick SiO₂ membrane on the top of the working volume. However the first sensors were prepared with a 1 μ m dia. capillary (Fig.14). This value was taken from the theoretical calculation because it should be sufficient to reach the targeted sensitivity.

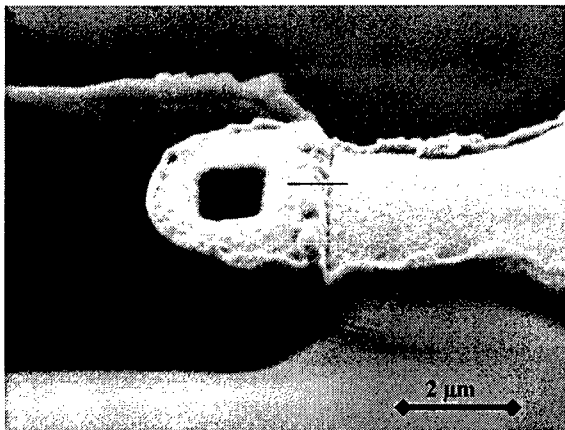


Figure 14: A micrograph of the detection capillary. The capillary has a diameter of only 1 μ m and is drilled by a focused ion beam trough the top electrode (coming from the right), the bottom electrode (coming from the left) and the supporting SiO₂ membrane. Top and bottom electrode are separated by an additional SiO₂ layer.

Prior to experiments with IR-radiation we have tested the basic response of the system to changes of the meniscus position in the capillary. This was done by gradually filling the working volume with an ionic liquid. Figure 15 shows the recorded data. The first both steps result from a partially filling of the working volume. Although the electrodes are not touched by the liquid, the signal amplitude increases du to capacitive coupling of the electrode connections via the SiO₂ membrane. The last step results from the wetting of the electrodes by the ionic liquid. From this data we have calculated a signal to noise ratio of 100 for the read out mechanism. This value is fully in accordance with the objectives of the project.

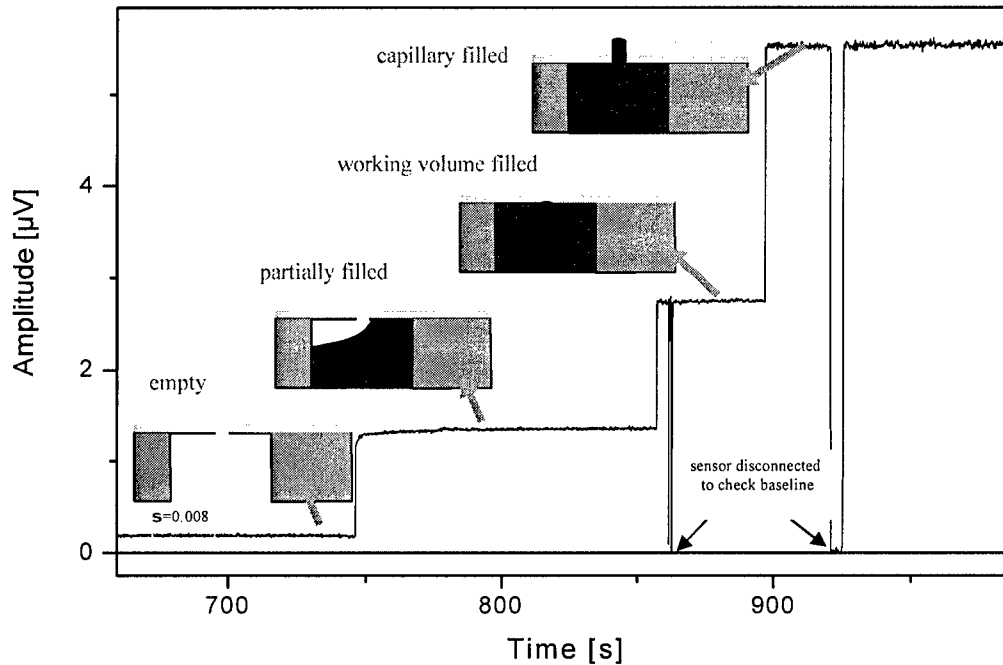


Figure 15: To test the response of the detection mechanism the sensor was gradually filled with an ionic liquid. The both first steps result from the partially filling of the working volume. The last step results from the wetting of the electrode surfaces in the capillary by the ionic liquid. A signal to noise ration of 100 could be estimated from this data.

To test the response to IR-radiation the sensor chip was mounted into a test setup an irradiated by a pulsed IR-Source. Figure 16 shows the typical response to a 2 second IR-pulse. The data clearly demonstrates that we have successfully transferred the biological IR-sensor concept from *Melanophila* into a technical sensor.

However for this first demonstrator the sensitivity is still 1-2 orders of magnitude less than the aimed sensitivity. The main reason for that is that we have intentionally omitted a thermal isolation of the sensor element in this first design. Our main aim was to prove the basic principle as fast as possible. The thermal isolation is a separate technological challenge therefore we decided to realize it in the second version of the sensor element.

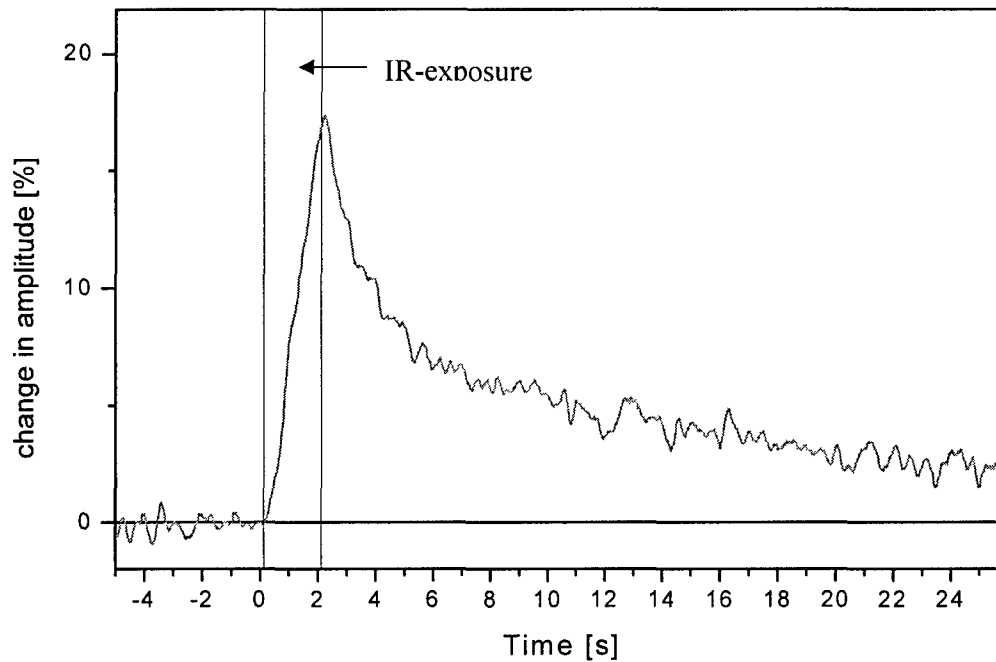


Figure 16: The relative sensor response for a 2 second pulse of IR-irradiation (yellow area). A 17% change has been obtained.

Publications:

A. Schmitz, A. Sehrbrock and H. Schmitz: The analysis of the mechanosensory origins of the infrared sensilla in *Melanophila acuminata* (Coleoptera: Buprestidae) gains new insight into the transduction mechanism. *Arthropod Structure & Development* [submitted for publication Sept 2006]

Patent Application: Infrared microsensor. German Patent Application No. 10 2006 002 177.0-52
(filed in January 2006)